



Polar mesospheric clouds observed by an iron Boltzmann lidar at Rothera (67.5°S, 68.0°W), Antarctica from 2002 to 2005: Properties and implications

Xinzhao Chu,¹ Patrick J. Espy,² Graeme J. Nott,^{2,3} Jan C. Diettrich,² and Chester S. Gardner⁴

Received 15 January 2006; revised 27 March 2006; accepted 30 June 2006; published 31 October 2006.

[1] Lidar observations of polar mesospheric clouds (PMC) were made at Rothera, Antarctica, from December 2002 to March 2005. Overall, 128 hours of PMC were detected among the 459 hours of observations, giving a mean occurrence frequency of 27.9%. The mean PMC centroid altitude is 84.12 ± 0.12 km, the mean PMC total backscatter coefficient is $2.34 \pm 0.11 \times 10^{-6} \text{ sr}^{-1}$, and the mean layer RMS width is 0.93 ± 0.03 km. The distribution of PMC centroid altitudes over all observations is symmetric (nearly Gaussian), with the most probable altitude (~ 84 km) near the center of the distribution. The distribution of PMC brightness is non-Gaussian and is dominated by weak PMC. The observed PMC altitudes at Rothera support the earlier lidar findings that Southern Hemispheric PMC are on average 1 km higher than corresponding Northern Hemispheric PMC, and higher PMC occur at higher latitudes. Significant interannual and diurnal variations are observed in PMC centroid altitude and brightness. Mean PMC altitude varies more than 1 km from one year to another. In addition, 24-hour, 12-hour, and 8-hour oscillations are clearly shown in PMC centroid altitude and brightness. The altitude distribution of PMC brightness peaks at a nearly constant altitude of 84 km, with weaker PMC found on either side of this altitude. The mean PMC altitudes averaged in brightness bins are anticorrelated with the PMC brightness, where weaker PMC occur at higher altitude and the PMC altitudes are proportional to the logarithm of the PMC brightness.

Citation: Chu, X., P. J. Espy, G. J. Nott, J. C. Diettrich, and C. S. Gardner (2006), Polar mesospheric clouds observed by an iron Boltzmann lidar at Rothera (67.5°S, 68.0°W), Antarctica from 2002 to 2005: Properties and implications, *J. Geophys. Res.*, *111*, D20213, doi:10.1029/2006JD007086.

1. Introduction

[2] Polar mesospheric clouds (PMC) and their visual manifestation, noctilucent clouds (NLC), have captured the interest of scientists around the world, as PMC/NLC are a potential indicator of long-term global climate change [Thomas, 1991]. They also provide a natural laboratory and an important tool for the study of the polar summer mesopause region. Observations have shown the water ice nature of PMC [e.g., Hervig et al., 2001]. Consequently, they are expected to be very sensitive to changes of mesospheric temperature, water vapor, and upwelling wind associated with the meridional circulation from the summer

pole to the winter pole. It has been suggested that long-term changes of mesospheric temperature and water vapor due to anthropogenic emission of CO₂ and CH₄ could cause long-term increases in PMC brightness or occurrence frequency [Thomas, 1991, 1996]. Although it is still debatable whether such evidence can be found in occurrence frequency [von Zahn, 2003; Thomas et al., 2003], recent SBUV studies seem to provide convincing evidence of an increase in PMC brightness over the last two decades [DeLand et al., 2003, 2006; Shettle et al., 2002]. However, PMC's role in monitoring global climate change is further complicated by the findings that space traffic may have contributed extra water vapor to the polar mesosphere and modified the PMC properties not only in the Arctic but also in Antarctica [Stevens et al., 2003, 2005a, 2005b]. To resolve these questions, the dynamical drivers of the background temperature and water vapor content of the atmosphere need to be quantified in both hemispheres, and the microphysical nucleation, growth and chemical processes of the PMC particles need to be ascertained.

[3] Significant progress has been made in recent years toward the understanding of the hemispheric differences in PMC and the related atmospheric dynamics, chemistry, and

¹Cooperative Institute for Research in Environmental Sciences and Department of Aerospace Engineering Sciences, University of Colorado, Boulder, Colorado, USA.

²Physical Sciences Division, British Antarctic Survey, Cambridge, UK.

³Now at Department of Physics and Atmospheric Science, Dalhousie University, Halifax, Nova Scotia, Canada.

⁴Department of Electrical and Computer Engineering, University of Illinois at Urbana-Champaign, Urbana, Illinois, USA.

microphysics. Recent analyses of decadal satellite data have provided new evidence of the hemispheric difference in PMC occurrence frequency, brightness, and extinction [DeLand *et al.*, 2003; Bailey *et al.*, 2005; Hervig and Siskind, 2006]. These provide a global picture of the earlier lidar finding of hemispheric difference in mean PMC altitude that was first reported by Chu *et al.* [2001a, 2001b, 2003, 2004a]. Modeling efforts addressing the causes of these hemispheric differences have suggested that hemispheric differences in solar flux [Chu *et al.*, 2003] and in the gravity wave driving of the mean flow [Siskind *et al.*, 2003, 2005] may be instrumental. The Thermosphere-Ionosphere-Mesosphere-Electrodynamics General Circulation Model (TIME-GCM) used by Chu *et al.* [2003] suggests that the summer mesopause temperature at the South Pole is colder than at the North Pole and the mesopause altitude (~ 91 km) at the South Pole is about 2 km higher than at the North Pole. However, the modeled mesospheric temperature in the PMC region between 80 and 87 km is warmer at the South Pole in summer [see Chu *et al.*, 2003, Figure 10]. These model predictions are being confirmed by new observational data. Recent studies using the HALOE data from the UARS satellite show that the Southern Hemisphere (SH) summer temperature at 80 km is warmer than the Northern Hemisphere (NH) [Hervig and Siskind, 2006]. More recently a study using the SABER data from the TIMED satellite shows that the SH summer mesopause is higher in altitude by about 2 km and colder in temperature by about 8 K than the NH (J. Xu *et al.* Mesopause structure from TIMED/SABER observations, submitted to *Journal of Geophysical Research*, 2006).

[4] Lidar observations at the South Pole have provided the first evidence of the removal of meteoric iron atoms by PMC ice particles [Plane *et al.*, 2004]. More lidar observations have provided further evidence of the removal of potassium and sodium atoms by PMC ice particles [Lübken and Höffner, 2004; Thayer and Pan, 2006]. These results suggest new aspects of heterogeneous chemistry in the atmosphere. Significant advances have also been made in the microphysical modeling of PMC and their relations to the surrounding atmospheric conditions [e.g., Jensen and Thomas, 1988; Klostermeyer, 1998; Rapp *et al.*, 2002; Berger and von Zahn, 2002; von Zahn and Berger, 2003; Rapp and Thomas, 2006]. These models are able to reproduce several general features of observed PMC and some details such as the tidal variations of PMC altitude and brightness [Berger and von Zahn, 2002; Klostermeyer, 2001]. However, many open questions remain concerning the microphysics and chemistry of PMC, as well as their interaction with atmospheric background conditions and dynamics. The resolution of these questions requires systematic high vertical resolution observations of PMC characteristics at a variety of latitudes in both the Northern and Southern hemispheres, particularly at the equatorward edges of the PMC region where the response to small changes is largest [Siskind *et al.*, 2005].

[5] Lidar observations of PMC are very valuable as they can provide high vertical resolution and high precision in determining PMC altitude, width, and brightness with full diurnal coverage. Multiple years of systematic lidar observations and studies of PMC have been reported for the South Pole (90°S) between 1999 and 2001 [Chu *et al.*,

2003], Andoya (69°N) between 1997 and 2001 [Fiedler *et al.*, 2003], and Sondrestrom (67°N) between 1994 and 2000 [Thayer *et al.*, 2003]. In addition, one season of lidar observations has been reported by Höffner *et al.* [2003] at Svalbard (78°N) for the year of 2001 and by Chu *et al.* [2004a] at Rothera (67.5°S) for the season of 2002–2003. Recently, a collaborative effort between the British Antarctic Survey and the University of Illinois has enabled the collection of three seasons of PMC data by an iron Boltzmann lidar at Rothera (67.5°S , 68.0°W), Antarctica from December 2002 to March 2005. Though the mean characteristics of the data from the first season (2002–2003) have been published by Chu *et al.* [2004a], systematic study of the three years of data provides a far more complete characterization of the PMC parameters, interannual, seasonal and diurnal variations as well as the relationship between the PMC altitude and brightness at this important southern location. In the following, we will briefly describe the instrumentation and data analysis at Rothera, and then present the observational results in four categories: mean characteristics, interannual and seasonal variations, diurnal variations, and the relationship of PMC altitude to brightness. Possible explanations for the observed PMC features will be discussed in the context of theoretical understanding and previous observations.

2. Instrumentation at Rothera and PMC Data Analysis

[6] Rothera (67.5°S , 68.0°W) is a British station located on Adelaide Island near the Antarctic Peninsula. The lidar observations at Rothera are a collaborative effort between the British Antarctic Survey and the University of Illinois. The instrument used to detect PMC at Rothera was the University of Illinois Fe Boltzmann temperature lidar, which made measurements at the South Pole from November 1999 to October 2001 [Chu *et al.*, 2001a, 2001b, 2003]. The operation principle and measurement capability of the Fe Boltzmann lidar have been described in considerable detail in previous publications [e.g., Chu *et al.*, 2002, 2003, 2004a]. For the Rothera observations, the lidar was integrated into a specially built laboratory that consisted of a lidar container hosting the lidar system and an office container hosting an electrical power transformer and working space. Each container has the standard dimensions of $6.1 \times 2.4 \times 2.6$ m for length, width, and height, respectively. This setup facilitated the relocation of an operational lidar system from Cambridge, UK to Rothera, Antarctica by a ship.

[7] The containerized lidar at Rothera was operated in the same configuration as at the South Pole. The lidar utilized two independent channels at 372 and 374 nm that were tuned to the Fe resonance transition lines originating from the lowest two sublevels of the ground state to an excited state [Chu *et al.*, 2002, 2003]. Raw data profiles were recorded at spatial resolution of 48 m and temporal resolution of 2.5 min (5000 shots at 33 Hz). A Hamming window with full width at half maximum (FWHM) of 960 m was applied to smooth photon counts in order to improve signal-to-noise ratio (SNR) [Chu *et al.*, 2004a]. After background subtraction and range-dependence removal, lidar profiles were integrated for each UT hour to further improve the

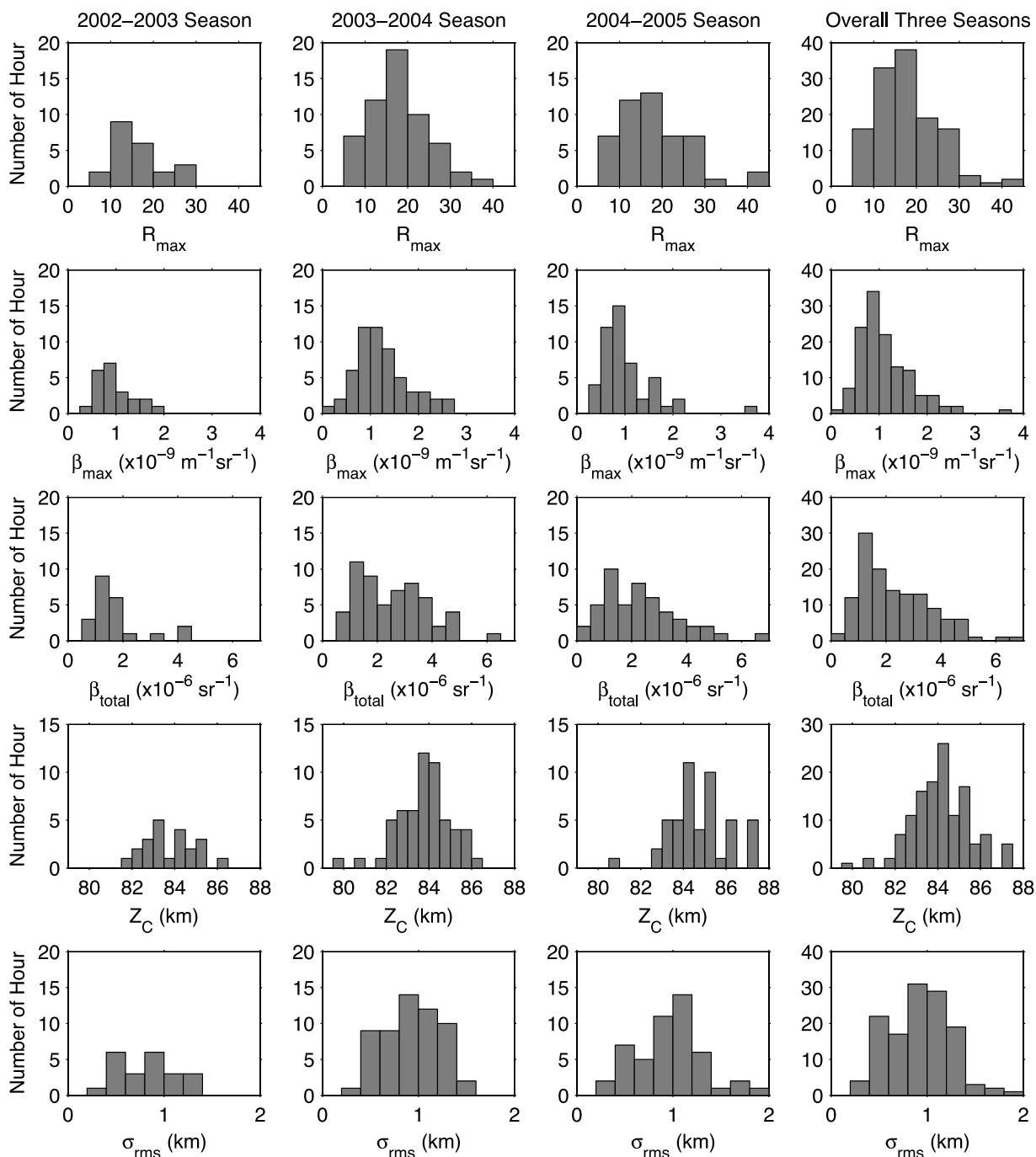


Figure 1. Histograms of PMC characteristics from 2002 to 2005 at Rothera, Antarctica. From top to bottom, the rows represent peak backscatter ratio R_{\max} , peak volume backscatter coefficient β_{\max} , total backscatter coefficient β_{total} , centroid altitude Z_C , and layer RMS width σ_{rms} . All PMC data points in each season and overall three seasons are used in the histograms.

SNR. The hourly data were then normalized to the Rayleigh (molecular scattering) signal at 50 km. PMC parameters were computed from the normalized profiles using a similar algorithm described in *Chu et al.* [2003]. The atmosphere number density, pressure, and temperature used in the computation were taken from the Mass Spectrometer Incoherent Scatter Extended (MSISE-00) model [*Picone et al.*, 2002]. Similar to the South Pole data analysis, PMC parameters were primarily derived from the 374 nm data

where contamination from the weaker Fe line is minimum. At the South Pole, because of extremely cold temperatures in summer (<150 K) and the strong PMC signal, the backscatter from the 374 nm Fe line in the PMC altitude range is typically less than 1% of PMC backscatter [*Chu et al.*, 2002, 2003]. However, some complication occurs at Rothera. As reported by *Chu et al.* [2004a] for the first summer season data, Rothera has much higher Fe density and lower Fe peak altitude in summer than the South Pole.

Table 1. Mean Characteristics of PMC Observed at Rothera, Antarctica, From 2002 to 2005^a

PMC Parameters	2002–2003	2003–2004	2004–2005	Overall
Peak backscatter ratio R_{\max}	15.9 ± 1.3 (6.1)	18.1 ± 0.93 (7.0)	18.4 ± 1.2 (8.1)	17.8 ± 0.64 (7.3)
Peak volume backscatter coefficient β_{\max} , × 10 ⁻⁹ m ⁻¹ sr ⁻¹	0.98 ± 0.08 (0.38)	1.24 ± 0.07 (0.55)	1.04 ± 0.08 (0.58)	1.12 ± 0.05 (0.55)
Total backscatter coefficient β_{total} , × 10 ⁻⁶ sr ⁻¹	1.76 ± 0.21 (0.96)	2.56 ± 0.17 (1.25)	2.34 ± 0.20 (1.39)	2.34 ± 0.11 (1.28)
Centroid altitude Z_C , km	83.74 ± 0.25 (1.17)	83.75 ± 0.16 (1.24)	84.73 ± 0.19 (1.35)	84.12 ± 0.12 (1.35)
Layer RMS width σ_{rms} , km	0.83 ± 0.06 (0.29)	0.93 ± 0.04 (0.29)	0.96 ± 0.05 (0.35)	0.93 ± 0.03 (0.32)
Layer FWHM, km	1.61 ± 0.09 (0.44)	1.96 ± 0.08 (0.61)	2.09 ± 0.12 (0.86)	1.95 ± 0.06 (0.71)
PMC examination hour	127	228	104	459
PMC occurrence hour	22	57	49	128
PMC occurrence frequency, %	17.3	25.0	47.1	27.9
PMC occurrence period	29 Dec 2002 to 26 Jan 2003 ^b	19 Nov 2003 to 2 Feb 2004	10 Dec 2004 to 14 Jan 2005 ^c	

^aFor each parameter, the first number is the mean value, the second number is the standard error of the mean, and the number in parentheses is the standard deviation of the distribution, i.e., the geophysical variability. All PMC data points in each season and overall three seasons are used in obtaining the mean PMC characteristics.

^bThe first observational day in this first season was 24 December 2002. There are no data before that.

^cAfter 15 January 2005, because of instrument problem, only one channel at 372 nm was running. These data have too much contamination from the Fe signal, so they are excluded in this study.

This causes considerable Fe contamination of the PMC signals even in the 374 nm data when it is on resonance. Fortunately, two independent channels of 372 and 374 nm allow us to estimate the 374 nm Fe signal and subtract it from the 374 nm data to derive the PMC signals. The scaling procedure used is described in detail in Appendix A. Lidar data were collected in several different modes: simultaneous 372 and 374 nm channels on resonance (including both Fe and PMC signals), 374 nm single channel off resonance (PMC only, without Fe signals), and 372 nm single channel on resonance (including PMC and Fe signals). Only both channel on-resonance and 374-nm-channel off-resonance data were used to identify PMC and derive their parameters.

[8] Three criteria are used to identify PMC as a distinct peak or peaks in the lidar data. The first is that the volume backscatter coefficient, $\beta(z)$, must be larger than 1.5 times the corresponding photon error, $\Delta\beta(z)$, in each bin within the full width at half maximum (FWHM) range of the peak: $\beta_{\text{PMC}}(z) > 1.5 \times \Delta\beta(z)$. The second is that the peak volume backscatter coefficient, β_{\max} , at altitude z_{\max} , must be at least twice as large as the photon counting error at the peak: $\beta_{\max} > 2\Delta\beta(z_{\max})$. Finally, the peak volume backscatter coefficient must be larger than 1.5 times the standard deviation of the background noise: $\beta_{\max} > 1.5 \times \text{stdnoise}$, where *stdnoise* represents the background noise. The *stdnoise* is computed as the standard deviation of background-subtracted, range-removed, volume backscatter coefficients in the range of 95–105 km. In addition, the clouds identified by the automated processing software using these criteria were verified visually using 2-D (time and altitude) smoothed contour plots of lidar backscatter coefficient profiles, where the PMC signals were evident.

3. Observations

[9] Lidar observations were made from December 2002 to early March 2005 at Rothera. PMC data were collected in three summer seasons during this period. The first PMC were observed on 29 December 2002, and the last one was recorded on 14 January 2005. In the following, we will present the statistical analysis of PMC mean characteristics, interannual, seasonal and diurnal variations. Finally, the

relationship between the PMC altitude and brightness will be examined.

3.1. Mean Characteristics of PMC

[10] Histograms of hourly mean PMC peak backscatter ratio R_{\max} , peak volume backscatter coefficient β_{\max} , total backscatter coefficient β_{total} , centroid altitude Z_C , and layer RMS width σ_{rms} are plotted in Figure 1 for each season as well as for overall three seasons together. The definitions of R_{\max} , β_{\max} , β_{total} , Z_C , and σ_{rms} can be found in Appendix A of *Chu et al.* [2003]. Table 1 summarizes the mean characteristics of Rothera PMC observed from 2002 to 2005. The data were averaged for each season (2002–2003, 2003–2004, 2004–2005) and for overall three seasons. For each parameter in Table 1, the first number is the mean value, the second number is the standard error of the mean, and the number in the parentheses is the standard deviation that represents the geophysical variability of each parameter. Both layer RMS width σ_{rms} and FWHM are listed in Table 1. The FWHM of PMC layer is ~ 2.1 times the layer RMS width σ_{rms} , which is slightly less than the ratio for a Gaussian distribution ($\text{FWHM}/\sigma_{\text{rms}} = \sqrt{8 \ln 2} \approx 2.35$).

[11] In the first season (2002–2003), lidar observations were made from 24 December 2002 to 10 February 2003. However, PMC only occurred for 22 hours from 29 December 2002 to 26 January 2003. During this 29-day-long occurrence period, a total of 127 hours of observations were used to examine PMC, giving an occurrence frequency of 17.3% for the season [*Chu et al.*, 2004a]. The second season (2003–2004) was a full season with observations starting in early November 2003 and extending through early March 2004. PMC occurred for 57 hours between 19 November 2003 and 2 February 2004. During this 76-day-long occurrence period, a total of 228 hours of observations were used to examine PMC, giving an occurrence frequency of 25.0% for the second season. During the third season (2004–2005), lidar observations were started in early November 2004, but PMC mode data ceased on 15 January 2005 because of an equipment failure. Although bad weather conditions at Rothera prevented data acquisition from 11 November to 9 December, PMC were observed for 49 hours from 10 December 2004 to 14 January 2005. During this 36-day-long occurrence period, a total of 104 hours of

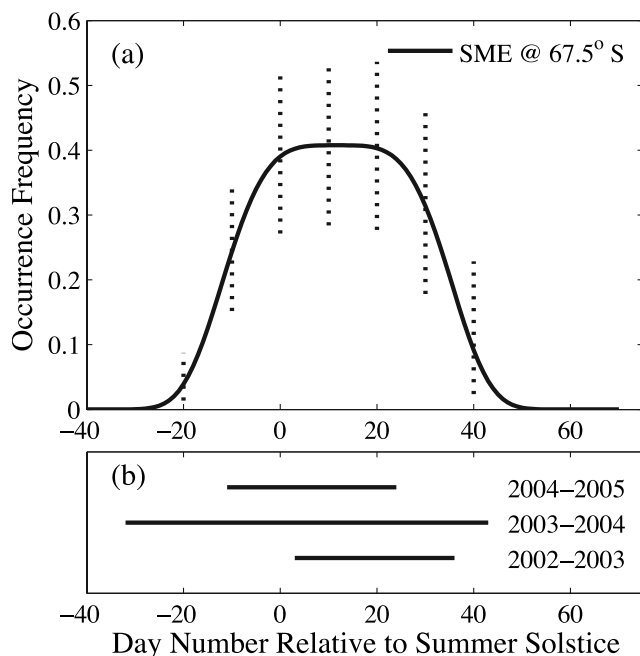


Figure 2. (a) PMC occurrence frequency derived from the SME climatology for the latitude of 67.5°S [Shettle *et al.*, 2002]. Vertical bars on the curve indicate the range of occurrence frequency from 65°S to 70°S (higher values correspond to 70°S). (b) PMC occurrence periods observed in three seasons at Rothera.

observations were used to examine PMC, giving a high occurrence frequency of 47.1%.

[12] To illustrate the locations on seasonal curve for data coverage in different seasons, the PMC occurrence frequency derived from the satellite SME climatology [Shettle *et al.*, 2002] is plotted in Figure 2 for the latitude of 67.5°S (top plot), along with the PMC occurrence periods observed at Rothera indicated by the horizontal bars in the bottom plot. The vertical bars on the SME curve indicate the range of occurrence frequency from 65°S to 70°S . Although the SME data were obtained nearly two decades ago, its climatology provides a typical seasonal variation of PMC occurrence near Rothera latitude. Figure 2 shows that the PMC data in 2003–2004 covered the full season while the data sets in 2002–2003 and 2004–2005 were mainly in the core period when the occurrence frequency is much higher than those at the beginning and the end of PMC seasons. Since the core period is included in all three seasons, the mean characteristics derived from these data represent the primary properties of Rothera PMC.

[13] Over three seasons, a total of 128 hours of PMC were observed during the 459 hours of total examination time, which gives a mean PMC occurrence frequency of 27.9% from 2002 to 2005. This overall mean occurrence frequency is significantly lower than the frequency observed at higher latitudes. An average occurrence frequency of 67.4% was reported at the South Pole (90°S) [Chu *et al.*, 2003], while the average at Svalbard (78°N) was 77% [Höffner *et al.*, 2003]. It is also lower than the 36% occurrence frequency observed at a similar northern latitude site, Andoya (69°N)

[Fiedler *et al.*, 2003], but much higher than the 11.8% reported at another similar northern latitude site, Sondrestrom (67°N) [Thayer and Pan, 2006].

[14] The mean centroid altitude of Rothera PMC from 2002 to 2005 is 84.12 ± 0.12 km. Although the standard deviation, which is a measure of the geophysical variability, is 1.35 km, the uncertainty quoted above is the standard error of the mean, 0.12 km, which indicates the uncertainty in the mean centroid altitude. This mean centroid altitude is ~ 0.8 km higher than the average observed at Andoya (69°N) [Fiedler *et al.*, 2003] and ~ 1.2 km higher than at Sondrestrom (67°N) [Thayer *et al.*, 2003]. However, it is still ~ 0.9 km lower than at the South Pole [Chu *et al.*, 2003]. This result supports the earlier findings of the hemispheric difference and latitudinal dependence of PMC altitudes. The southern PMC are ~ 1 km higher than the northern clouds observed at similar latitudes, and PMC are generally higher at higher latitudes [Chu *et al.*, 2004a]. To better illustrate this result, Figure 4 of Chu *et al.* [2004a] was revised and plotted in Figure 3 to reflect the updated PMC mean altitudes obtained by lidar observations in multiple seasons at Rothera and Davis (68.6°S , 78.0°E), Antarctica. The other data points are the same as in the original figure. (See Chu *et al.* [2004a] for references.) The Rothera point (84.12 ± 0.12 km) is updated using the mean centroid altitude over all three seasons from the current

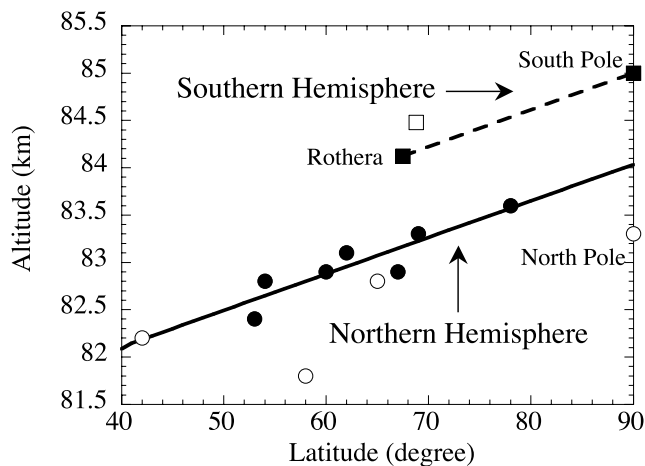


Figure 3. Interhemispheric comparison of the PMC altitude versus latitude, revised from Figure 4 of Chu *et al.* [2004a]. Circles are for the Northern Hemisphere and squares are for the Southern Hemisphere. Filled circles indicate large data sets and are used to obtain the linear fit (solid line) to the northern PMC altitudes. Open circles indicate limited data sets and are excluded in the fit. The open square is for the Davis data. The Rothera and Davis data points are updated using PMC mean centroid altitudes obtained by lidar observations in multiple seasons (three seasons from 2002 to 2005 for Rothera and three seasons from 2001 to 2004 for Davis) at these two stations (see text for details). Other data points are the same as in the original figure [see Chu *et al.*, 2004a, for references]. The linear line fitted to the Northern Hemisphere data points has a slope of 39 ± 8 m/deg with a correlation coefficient of 90.7%, and the linking line between Rothera and the South Pole gives a slope of 39 m/deg.

paper. The Davis data point (84.48 ± 0.19 km) is updated using the lidar data obtained by Andrew Klekociuk of the Australian Antarctic Division from 2001 to 2004, which was previously reported at the LPMR 2004 workshop [Chu *et al.*, 2004b]. Because of the limited number of PMC observations at Davis, the Davis point is not used to fit the southern PMC altitudes. The Davis measurement is plotted to illustrate the consistency of this limited data set with the more extensive Rothera and South Pole measurements. The PMC mean centroid altitude at Davis is about 0.28 km above the dashed line linking the Rothera and South Pole means. Figure 3 clearly shows that the Southern Hemisphere and Northern Hemisphere lines are nearly parallel to each other and the southern line of PMC altitudes is higher than the northern line by about 1 km. It is also clear from Figure 3 that higher PMC occur at higher latitudes in both hemispheres with an ascending rate of 39 ± 8 m/deg.

[15] As shown in Figure 1, the distribution of the PMC centroid altitude over the three seasons at Rothera is effectively Gaussian with the most probable altitude in the range of 84–84.5 km (see section 4.2 for detailed discussions on the distribution). Thus the mean, standard error of the mean, and the standard deviation are well defined, and the differences noted above are statistically significant. Figure 1 also demonstrates that the PMC distributions for the individual seasons are not noticeably Gaussian because of the low number of samples in each seasons. This is especially true in the first season when only 22 hours of PMC were detected. However, the additional samples used in overall average yield a PMC distribution that is effectively Gaussian with a geophysical variability that is similar to that observed in each season.

[16] The mean layer RMS width of PMC is 0.93 ± 0.03 km at Rothera, which is $\sim 20\%$ larger than the PMC layers (0.75 km) at the South Pole [Chu *et al.*, 2003]. The RMS width obtained at Rothera equates to a FWHM of ~ 2 km that may be compared to the FWHM of PMC layers observed at Sondrestrom and Andoya of 1 and 1.2 km, respectively [Thayer *et al.*, 2003; Fiedler *et al.*, 2003]. Thus Rothera PMC layer width would appear to be nearly twice that found at similar latitudes in the Northern Hemisphere. However, differences in the data processing approaches used at these four locations could contribute to the observed PMC width differences. For example, the Hamming smoothing width used at Rothera, 960 m, is larger than that used for the data from the South Pole (250 m). Our examination shows that using a Hamming window of 250 m on the Rothera data decreases the resulting RMS width by $\sim 15\%$, yielding a RMS thickness of 0.79 km that is similar to that found at the South Pole. However, this is still 50% larger than the northern PMC width obtained at Sondrestrom and Andoya where the bin widths used in the data processing are respectively 384 and 150 m, comparable to the Hamming smooth width (250 m). Another contributing factor could be the 1-hour integration time used at Rothera and the South Pole, compared with the much shorter integration times used at Sondrestrom (10 min) and Andoya (14 min). Since the PMC layer altitude may vary in time, longer integrations would interpret these altitude variations as an increase of layer width. Our examination on the 2.5-min resolution PMC contour plots indicates that although this does occur when the PMC

layers are changing rapidly, they typically remain at a relatively constant altitude on timescales of an hour. The effect of longer integration times on the overall mean RMS width would appear not to exceed 20%, yielding a conservative estimate that the Rothera PMC layer width is about 30% larger than northern PMC at similar latitudes.

[17] The mean PMC brightness expressed as total backscatter coefficient β_{total} is $2.34 \pm 0.11 \times 10^{-6}$ sr $^{-1}$ at Rothera, which is less than half of the brightness observed at the South Pole ($5.45 \pm 0.19 \times 10^{-6}$ sr $^{-1}$) [Chu *et al.*, 2003]. The distribution of Rothera PMC brightness is non-Gaussian and dominated by weak PMC. As shown in Figure 1, the most probable β_{total} is in the range of 1.0 – 1.5×10^{-6} sr $^{-1}$, which is about half of the mode value observed at the South Pole (2 – 3×10^{-6} sr $^{-1}$) [Chu *et al.*, 2003]. The distribution of PMC brightness at the South Pole is also non-Gaussian and dominated by weak PMC. The mean peak backscatter ratio R_{max} at Rothera is 17.8 ± 0.64 , and the mean peak volume backscatter coefficient β_{max} is $1.12 \pm 0.05 \times 10^{-9}$ m $^{-1}$ sr $^{-1}$. Both of these mean values are less than one third of that measured at the South Pole PMC [Chu *et al.*, 2003]. However, as the PMC at Rothera occur at lower altitudes than those at the South Pole, the Rayleigh backscatter coefficient from the background atmosphere density is higher and results in a lower PMC backscatter ratio. In addition, the larger smoothing window used at Rothera contributes to a smaller peak backscatter ratio and peak volume backscatter coefficient but a larger PMC layer RMS width. As the total backscatter coefficient is an integration of PMC volume backscatter coefficient through the PMC layer altitude range (i.e., proportional to the product of the peak volume backscatter coefficient and the layer RMS width), it remains unchanged for different smoothing or bin widths. Since the total backscatter coefficient is not affected by the background atmosphere or smoothing width, it provides a better ground for comparison between different lidar or satellite observations.

[18] To compare Rothera PMC brightness, expressed as total backscatter coefficient, with lidar data collected in the Northern Hemisphere at different wavelengths, the PMC ice particle size and density distribution has to be adopted in order to derive the color ratios. From Höffner *et al.* [2003] we assume a lognormal size distribution of spherical ice particles with a median radius of $r_m = 40$ nm and a width of $\sigma = 1.4$. The resultant color ratios are 2.28 for 374 nm/532 nm, and 7.3 for 374 nm/770 nm [Höffner *et al.*, 2003]. Here, 532 nm is used for the Rayleigh lidars at Sondrestrom and Andoya, and 770 nm is used for the potassium lidar at Svalbard. Furthermore, since the total backscatter coefficients are not given for Andoya and Svalbard by Fiedler *et al.* [2003] and Höffner *et al.* [2003], a Gaussian peak is assumed for the PMC layer; thus the total backscatter coefficient β_{total} at the original 532 and 770 nm is approximated from the peak volume backscatter coefficient β_{max} and the layer FWHM using the following equation:

$$\beta_{\text{total}} = \sqrt{2\pi} \cdot \beta_{\text{max}} \cdot \frac{\text{FWHM}}{\sqrt{8 \ln 2}}. \quad (1)$$

These total backscatter coefficients are then converted to those observed at 374 nm using the color ratios given

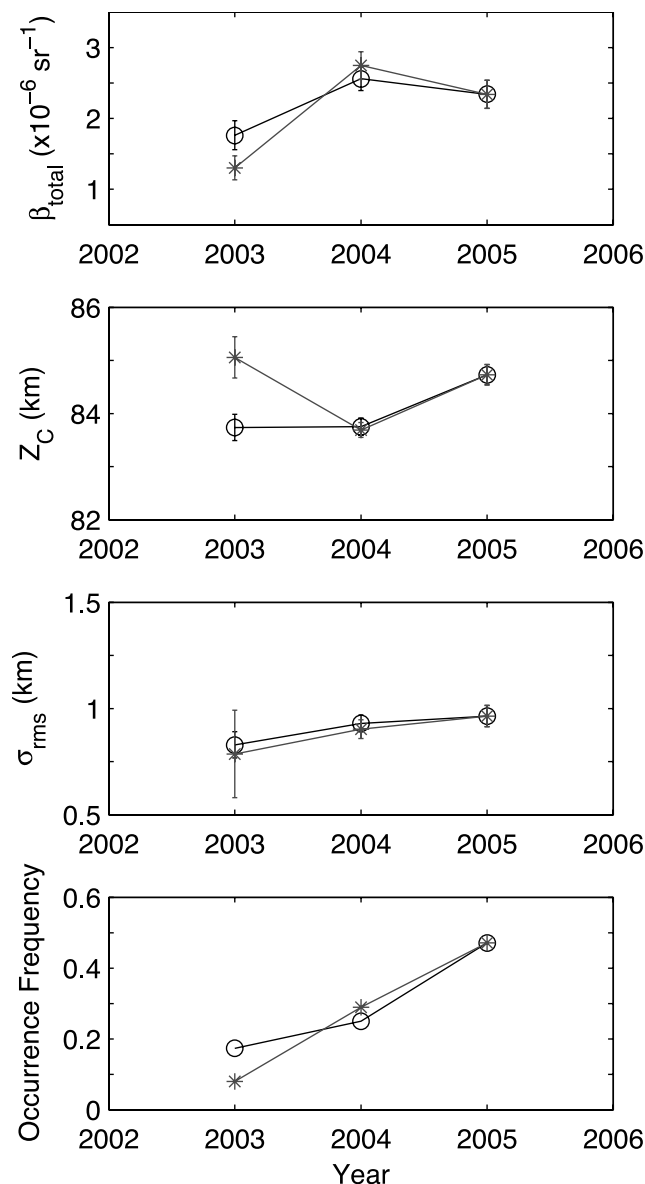


Figure 4. Interannual variations of PMC total backscatter coefficient, centroid altitude, layer RMS width, and occurrence frequency from 2002 to 2005 at Rothera. Circles represent the seasonal means in each season, and asterisks represent the means in the central period from -11 day to $+24$ day in each season. The error bars are the standard errors of the means.

above. The resulting mean total backscatter coefficients at 374 nm are $2.48 \times 10^{-6} \text{ sr}^{-1}$ for Sondrestrom (67°N), $2.80 \times 10^{-6} \text{ sr}^{-1}$ for Andoya (69°N), and $5.15 \times 10^{-6} \text{ sr}^{-1}$ for Svalbard (78°N). Thus the total brightness of PMC at Rothera is only slightly lower than the similar latitude sites at Sondrestrom and Andoya, but more than a factor of 2 less than the high-latitude site at Svalbard.

3.2. Interannual and Seasonal Variations of PMC

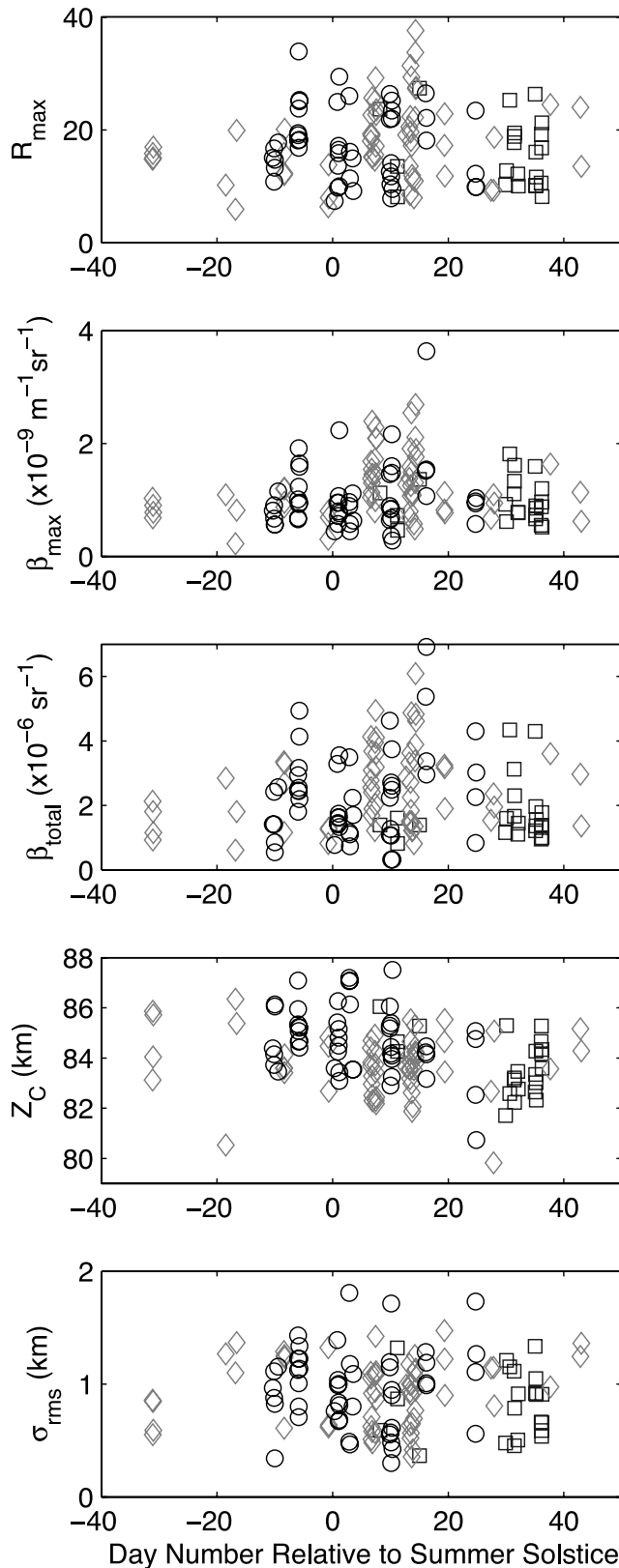
[19] There are considerable interannual and seasonal variations in PMC altitude and brightness at Rothera. To illustrate the interannual variations, the seasonal means of

PMC brightness β_{total} , altitude Z_C , RMS width σ_{rms} , and occurrence frequency are plotted versus year in Figure 4 (circles). However, as illustrated in Figure 2, except the second season covering a full PMC season, the first and the third seasons were incomplete because of either weather or instrument problems. Thus the comparison of seasonal means may not be representative as data were collected in different periods. To address this, a common observational period extending from -11 days to $+24$ days relative to the summer solstice (10 December to 14 January) was selected for all three seasons. This period spans about 36 days (5 weeks), and is the central part of austral PMC seasons. Means obtained in this period for different years are plotted as asterisks in Figure 4. PMC occurrence hours during this central period are 4 hours out of 50 hours, 44 hours out of 152 hours, and 49 hours out of 104 hours of observations for the first, second, and third seasons, respectively. This gives 8%, 28.9%, and 47.1% of occurrence frequency in the central part of the 2002–2003, 2003–2004, and 2004–2005 PMC seasons. During the central period, the 2004–2005 season has a much higher occurrence frequency than the other two seasons, while the 2002–2003 season has an exceptionally low occurrence frequency. Supporting this latter finding, a 532-nm Rayleigh lidar at Australian Davis Station (68.5°S , 78.0°E) in Antarctica also detected little PMC activity in the central period of the same 2002–2003 PMC season (A. Klekociuk, Australian Antarctic Division, private communication, 2003). Although the entire 2002–2003 season at Rothera yields an overall occurrence frequency of 17.3% [Chu *et al.*, 2004a], most of the PMC (18 hours) occurred after 19 January 2003, and thus outside the core period considered here. The study of Stevens *et al.* [2005b] shows that the enhanced PMC occurrence during the late season may have been caused by the main engine exhaust ($\sim 98\%$ being water) from the Columbia Space Shuttle (launched on 16 January 2003) reaching Antarctica and carrying extra water vapor into this region.

[20] During the central period, the first season has the highest centroid altitude, $85.06 \pm 0.39 \text{ km}$, but the smallest total backscatter coefficient, $1.30 \pm 0.17 \times 10^{-6} \text{ sr}^{-1}$. On the other hand, the second season has the lowest centroid altitude, $83.69 \pm 0.14 \text{ km}$, but the strongest brightness, $2.75 \pm 0.19 \times 10^{-6} \text{ sr}^{-1}$. The PMC during the third season (also the central period) have a mean centroid altitude of $84.73 \pm 0.19 \text{ km}$ similar to the first season, but a mean brightness of $2.34 \pm 0.2 \times 10^{-6} \text{ sr}^{-1}$, which is comparable to the second season. Because of the extremely low occurrence frequency, only 4 hours of PMC data were recorded during the central period in the first season (2002–2003). Thus the statistic significance of the results in the first season is low and it is more appropriate to compare the PMC properties in the second and the third seasons for the interannual variation study. It is striking that the PMC centroid altitude exhibits a change of more than 1 km from 2003–2004 to 2004–2005. This is similar to the $\sim 1 \text{ km}$ interannual variation observed over two seasons at the South Pole [Chu *et al.*, 2003].

[21] It is also important to assess the influence of uneven diurnal sampling of PMC data on the interannual variations, in light of large diurnal variations observed in PMC centroid altitude and brightness at Rothera as described in section 3.3. The PMC centroid altitudes are averaged in each local hour

for the 2003–2004 season, and then the diurnal harmonic fit used in section 3.3 is applied to the obtained 21 hours of samples among 24-hour diurnal cycle. The mean centroid altitude (i.e., A_0 in equation (2) of section 3.3) derived from the harmonic fit is 83.77 ± 0.13 km for 2003–2004.



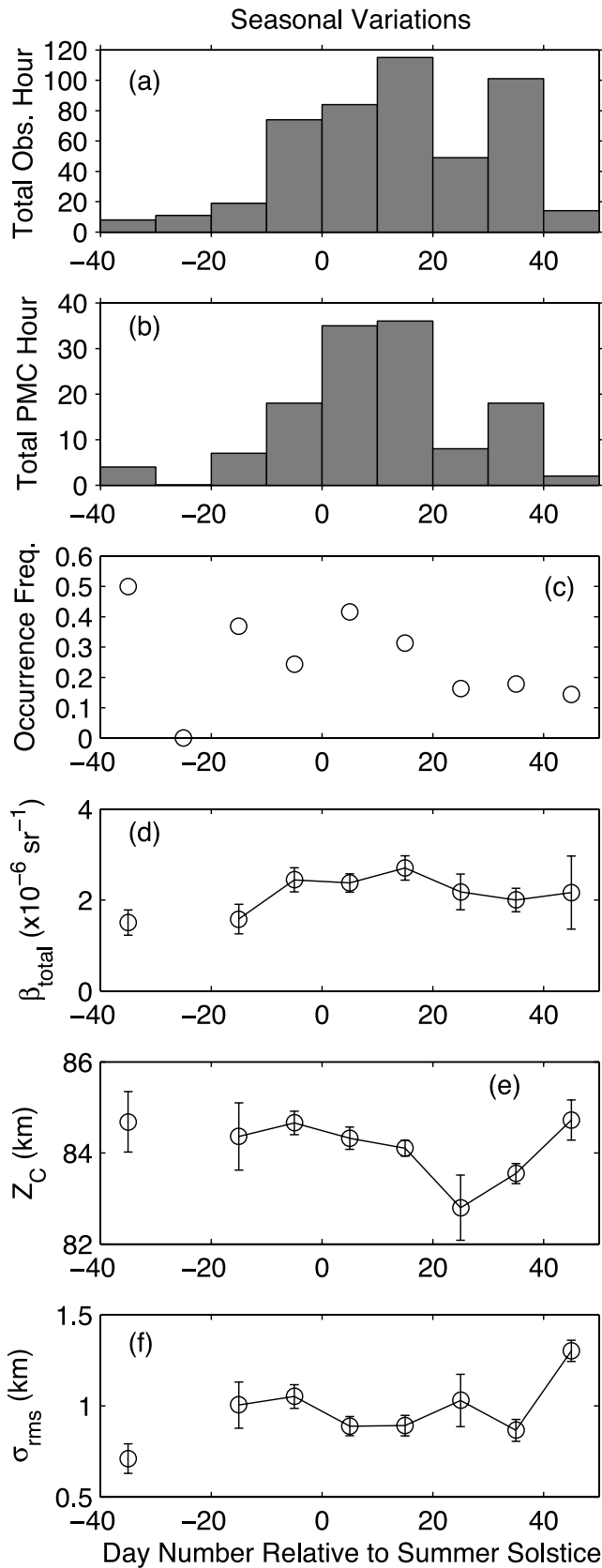
Similar approach is applied to the 2004–2005 season data that cover 20 hours of diurnal samples and the derived mean centroid altitude is 84.50 ± 0.22 km. Thus the mean centroid altitudes derived from the diurnal harmonic fits show an interannual variation of ~ 0.7 km, which is slightly smaller than the difference derived from seasonal means, but still significant enough to indicate the large interannual variations in PMC centroid altitude. The diurnal harmonic fits to the PMC brightness in the 2003–2004 and 2004–2005 seasons show essentially the same mean brightness in these two seasons. This result is similar to the situation indicated by the seasonal means of PMC brightness; that is, there are no large interannual variations in PMC brightness between these two years.

[22] The seasonal variations of hourly mean PMC parameters are plotted versus day number relative to summer solstice (21 December) in Figure 5. Data in different seasons are represented by different symbols in order to illustrate PMC variations in each season. Large changes in PMC brightness, altitude, and RMS width are exhibited on each observational day, which are associated with the strong diurnal variations described in section 3.3. The limited data points are not sufficient to study the seasonal trend for each individual season. To improve the statistics, all data over the three seasons are put together to derive a mean seasonal trend as shown in Figure 6. The PMC season was divided into 9 periods with a 10-day duration for each period. The total observational hours and the PMC occurrence hours are plotted in the top two panels. The ratio of PMC occurrence hours to the total observational hours defines the occurrence frequency. The higher occurrence frequencies from -40 to -30 days and from -20 to -10 days are most likely caused by the low sample numbers, and thus may not be representative. We will only look at the central period of the PMC season when there are at least 40 hours of observations available, which extends from -10 to $+40$ days. The occurrence frequency peaks in the period of 0 – 10 days after the summer solstice ($\sim 40\%$), with lower occurrence frequency on either side of the season. The means of the PMC brightness, centroid altitude, and layer RMS width are illustrated in the bottom three panels. During the period from -10 to $+40$ days when the number of data is sufficient, the PMC centroid altitude decreases from its maximum around the summer solstice to a minimum around 20 – 30 days after the solstice, and then increases again. The variations of PMC brightness are not clear through the season and the total backscatter coefficient is relatively constant around $2.3 \times 10^{-6} \text{ sr}^{-1}$ from -10 day to $+30$ day. Similarly, no clear trend is shown for the seasonal variations of the layer RMS width.

Figure 5. Seasonal variations of PMC parameters along the day number relative to summer solstice (21 December) for each season at Rothera. Squares are for the first season (2002–2003), diamonds are for the second season (2003–2004), and circles are for the third season (2004–2005). From top to bottom, the plots represent peak backscatter ratio R_{max} , peak volume backscatter coefficient β_{max} , total backscatter coefficient β_{total} , centroid altitude Z_C , and layer RMS width σ_{rms} .

3.3. Diurnal Variations in PMC

[23] The lidar observations at Rothera covered 24-hour full diurnal cycle, allowing the study of PMC diurnal variations. In Figure 7, total observational hours, PMC



occurrence hours, and occurrence frequency are plotted against local time. Local time (LT) at Rothera is equal to universal time (UT) minus 4.5 hours, i.e., $LT = UT - 4.5$ hours. Thus local midnight at Rothera is 4.5 UT, and local noon is 16.5 UT. Figure 7 shows that the observational time in each local hour have a minimum of 10 hours and a maximum of 25 hours. PMC were recorded in every local hour with a minimum of 2 hours and a maximum of 9 hours. The overall occurrence frequency of all PMC regardless their brightness is illustrated as open circles in Figure 7c. It peaks around 5–6 LT (~55%), and is lowest around 14 LT (~10%). For the rest of the day, it varies around 25% with fluctuations on the order of 10%. In the study of the PMC diurnal variations, the sinusoidal variation of solar background at Rothera must be considered. Shown in Figure 7d is a typical solar background photon count recorded by the lidar at Rothera. In contrast to the constant solar background over a day at the South Pole, Rothera solar background varies strongly with local time. While the background at midnight is low enough to be negligible, it is nonnegligible around local noon and the background effect must be taken into account. The detection efficiency at midnight is clearly much better than the efficiency around noon. This allows weak PMC to be detected by the lidar during midnight but missed around noon. To distinguish the true geophysical diurnal variations from the detection efficiency effect driven by solar background, stronger PMC were separated from weaker PMC and the occurrence frequency for these stronger PMC were computed. Here, β_{total} of $2 \times 10^{-6} \text{ sr}^{-1}$ is used as the limit to divide the PMC brightness as clouds brighter than this are well above detection threshold for noontime solar scattering conditions. The resulted occurrence frequency for stronger PMC is illustrated as the asterisks in Figure 7c. The maximum frequency of bright PMC occurs at 6 LT with a frequency of ~30%. Between 18 and 21 LT, the occurrence frequency of bright PMC is significantly lower than the overall occurrence frequency in the same hours, and appears to have the minimum frequency of ~5% for bright PMC. It should be noted that the peaks of both the overall occurrence frequency and the bright PMC occurrence frequency are not locked to local midnight. This indicates that the observed diurnal variations of occurrence frequency are most likely caused by the true geophysical variations and not by the sinusoidal variation of the solar background.

[24] To illustrate the diurnal behavior of PMC parameters, three seasons of individual hourly measurements of PMC total backscatter coefficient, centroid altitude, and RMS width are shown as scatterplots against local time in the leftmost column of Figure 8. Although some diurnal variation may be shown in the brightness and altitude, large fluctuations remain within each hour bin. To smooth out

Figure 6. Average seasonal variations over the three seasons from 2002 to 2005: (a) total observational hours, (b) total PMC occurrence hours, (c) PMC occurrence frequency, (d) mean total backscatter coefficient, (e) mean centroid altitude, and (f) mean layer RMS width in each 10-day period as a function of day number relative to summer solstice. The error bars are the standard errors of the means, representing the uncertainties of the means.

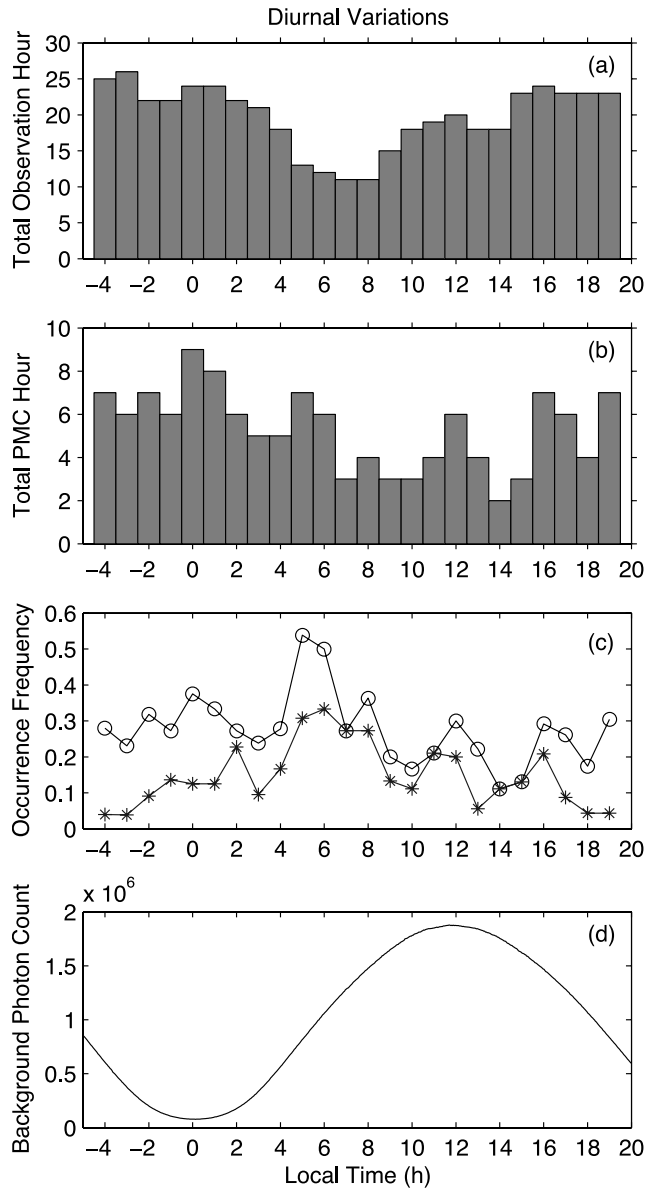


Figure 7. Diurnal distribution of (a) total observational hours, (b) total PMC occurrence hours, and (c) PMC occurrence frequency as a function of local time. (All PMC data points in overall three seasons are used in the plots.) In Figure 7c, the circles are for all PMC regardless of brightness, and asterisks are for PMC with $\beta_{\text{total}} > 2 \times 10^{-6} \text{ sr}^{-1}$. (d) Background photon counts (from 140 to 190 km for 5000 shots) recorded by the lidar on 2–3 January 2004 at Rothera, showing large sinusoidal variations with local time.

these large fluctuations, PMC brightness and altitude data are averaged in each local hour (regardless of their brightness) and plotted in the column second from the left. The vertical bars represent the 95% confidence intervals of the mean values, i.e., 2 times of the standard errors of the means in each local time hour. It is obvious from the overall averaged data that the altitude reaches a maximum around 19 LT, while the brightness is minimum at that time. To analyze the components in the diurnal variations, harmonic

fits consisting of 24-hour, 12-hour, and 8-hour oscillations given by equation (2) were applied to the averaged brightness and altitude, using the approach similar to *Chu et al.* [2001b, 2003]:

$$y = A_0 + A_{24} \cos \left[\frac{2\pi}{24} (t - \Phi_{24}) \right] + A_{12} \cos \left[\frac{2\pi}{12} (t - \Phi_{12}) \right] + A_8 \cos \left[\frac{2\pi}{8} (t - \Phi_8) \right]. \quad (2)$$

Fitting results are plotted as the solid curves in the column second from the left and fitting parameters are listed in Table 2. Our test of a 6-hour oscillation fit to the data shows that the amplitude of 6-hour component is not significant, so not shown in this paper. All fitted components in equation (2) to the overall PMC centroid altitude are significant as indicated by the high correlation coefficient (88.7%) and small relative errors. However, the errors are larger and the correlation is less when fitted to the PMC brightness. It is obvious from Table 2 that the 24-hour diurnal oscillations dominate the overall averaged brightness and altitude at Rothera. While 12-hour semidiurnal and 8-hour terdiurnal variations are much weaker in the overall averaged brightness, strong 8-hour terdiurnal oscillation occurs in PMC altitude. The amplitude of 8-hour oscillation in altitude doubles the amplitude of 12-hour oscillation. The presence of a strong terdiurnal component in the Rothera PMC is quite different from the situations observed at Andoya [*von Zahn et al.*, 1998; *Fiedler et al.*, 2005] and the South Pole [*Chu et al.*, 2001b, 2003]. At these two stations there is no obvious 8-hour oscillation observed in the multiple year-averaged PMC brightness and altitude (7 years for Andoya [*Fiedler et al.*, 2005] and 2 years for the South Pole [*Chu et al.*, 2003]), although 8-hour oscillations were shown in individual years like 1998 and 2000 at Andoya [*Fiedler et al.*, 2005] and in a continuous 26 hours of observations at the South Pole [*Chu et al.*, 2003]. Both the diurnal and semidiurnal variations are substantially responsible for the local time variations of altitude and brightness averaged over multiple years at the South Pole and Andoya [*Chu et al.*, 2003; *Fiedler et al.*, 2005]. The weak semidiurnal but strong terdiurnal oscillations seem to be a unique feature at Rothera and parallel the climatology of tides seen in the MF radar winds at Rothera, where the 12-hour oscillation does not dominate the zonal and meridional winds but a significant 8-hour oscillation is seen in both winds during the summer seasons between 80 and 95 km, which is not observed at other Antarctic stations (R. E. Hibbins et al., A climatology of tides and gravity wave variance in the MLT above Rothera, Antarctica, submitted to *Journal of Atmospheric and Solar-Terrestrial Physics*, 2006). As shown by the phases listed in Table 2, there is an anticorrelation between the brightness and altitude in the overall average for all fitted components. The phase differences between the brightness and altitude are 10.2 ± 1.3 hours for the diurnal, 5.3 ± 1.8 hours for the semidiurnal, and 3.1 ± 2.3 hours for the terdiurnal oscillations, within what would be expected for complete anticorrelation (12 hours, 6 hours, and 4 hours for the components, respectively).

[25] Similar to the analysis of the PMC occurrence frequency, we separated stronger PMC from weaker PMC,

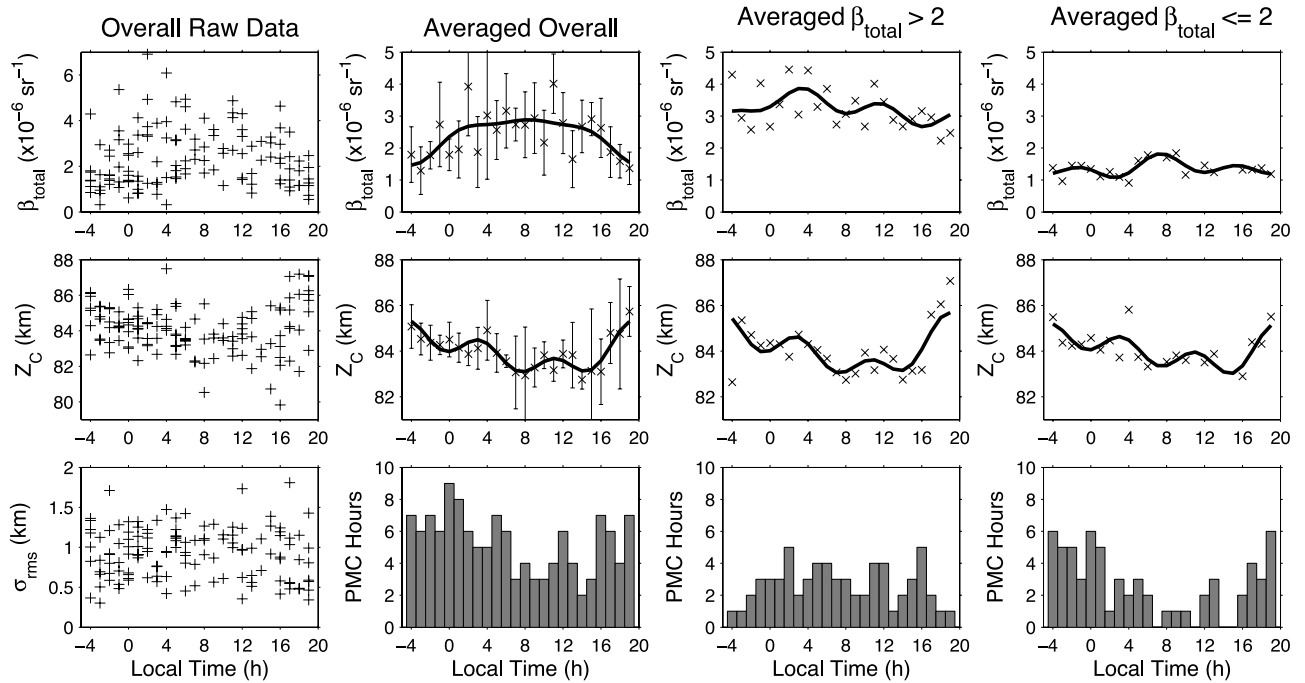


Figure 8. Diurnal variations of (top) PMC total backscatter coefficient and (middle) altitude. (bottom) PMC RMS width and PMC occurrence hours. (All PMC data points in overall three seasons are used in the plots.) The first column shows the raw data points in each hour, the second column gives the average in each hour regardless of PMC brightness, the third column is the average for stronger PMC ($\beta_{\text{total}} > 2 \times 10^{-6} \text{ sr}^{-1}$), and the fourth column is the average for weaker PMC ($\beta_{\text{total}} \leq 2 \times 10^{-6} \text{ sr}^{-1}$). Solid curves are the harmonic fittings consisting of 24-hour, 12-hour, and 8-hour oscillations given by equation (2). The vertical bars in the second column represent the 95% confidence intervals of the mean values, i.e., 2 times the standard errors of the means.

and then took averages in each LT hour for the strong and weak PMC, respectively. Again, β_{total} of $2 \times 10^{-6} \text{ sr}^{-1}$ is used as the limit to divide the PMC brightness. Averaged results are shown in the third (for strong PMC) and fourth (for weak PMC) columns of Figure 8. Notice that the weak PMC mainly occur from 17 LT through midnight, which indicates the influence of the solar background variation. Our fitting treatment below is for comparison purpose. The diurnal parameters derived from the strong PMC case are more reliable than from the weak PMC case. Harmonic fits given by equation (2) were applied to these data. The fitting results are shown as the solid curves in Figure 8 and the fitting parameters are listed in Table 2. The major difference is the increased 8-hour amplitude in brightness for both the strong and weak PMC cases. Because of the opposite phase of the 8-hour oscillations in the strong and weak PMC cases, they nearly cancel each other and are therefore only

weakly observed in the overall brightness averages shown in the second column of Figure 8. The 24-hour and 8-hour components are clearly observed in the PMC altitude for both the strong and weak PMC cases. However, now the phase of these components does not change for the strong and weak cases, which gives strong 24- and 8-hour signatures in the overall average shown in the second column of Figure 8. The 8-hour oscillations in brightness and altitude are in phase for strong PMC but out of phase for weak PMC. On the other hand, the 24-hour and 12-hour oscillations exhibit opposite phases between brightness and altitude for both the strong and weak PMC cases. Even after separating the strong PMC from the weak ones, the diurnal variation is still clearly shown in the PMC altitude. Also, we notice that neither the brightness peak nor the altitude peak is locked to the local midnight or local noontime. These indicate that the diurnal variations of

Table 2. Fitting Parameters of the Harmonic Fits to the Overall Averaged, the Stronger, and the Weaker PMC in Figure 8

	Overall Averaged PMC		Stronger PMC		Weaker PMC	
	$\beta_{\text{total}}, \times 10^{-6} \text{ sr}^{-1}$	$Z_C, \text{ km}$	$\beta_{\text{total}}, \times 10^{-6} \text{ sr}^{-1}$	$Z_C, \text{ km}$	$\beta_{\text{total}}, \times 10^{-6} \text{ sr}^{-1}$	$Z_C, \text{ km}$
A_0	2.41 ± 0.13	83.98 ± 0.08	3.24 ± 0.13	84.07 ± 0.19	1.37 ± 0.05	84.04 ± 0.14
A_{24}	0.61 ± 0.19	0.75 ± 0.12	0.36 ± 0.19	0.86 ± 0.26	0.15 ± 0.06	0.62 ± 0.20
A_{12}	0.24 ± 0.19	0.24 ± 0.12	0.13 ± 0.19	0.34 ± 0.26	0.14 ± 0.07	0.24 ± 0.20
A_8	0.10 ± 0.19	0.52 ± 0.12	0.23 ± 0.19	0.58 ± 0.26	0.18 ± 0.07	0.54 ± 0.21
Φ_{24}	7.93 ± 1.19	-2.25 ± 0.61	4.02 ± 1.96	-2.94 ± 1.17	8.97 ± 1.73	-1.27 ± 1.23
Φ_{12}	1.90 ± 1.50	7.19 ± 0.94	1.31 ± 2.78	6.24 ± 1.51	7.58 ± 0.90	7.99 ± 1.52
Φ_8	0.16 ± 2.33	3.24 ± 0.29	3.70 ± 1.03	2.78 ± 0.58	-0.81 ± 0.42	3.23 ± 0.43
Correlation coefficient, %	64.8	88.7	50.4	70.8	75.2	75.1

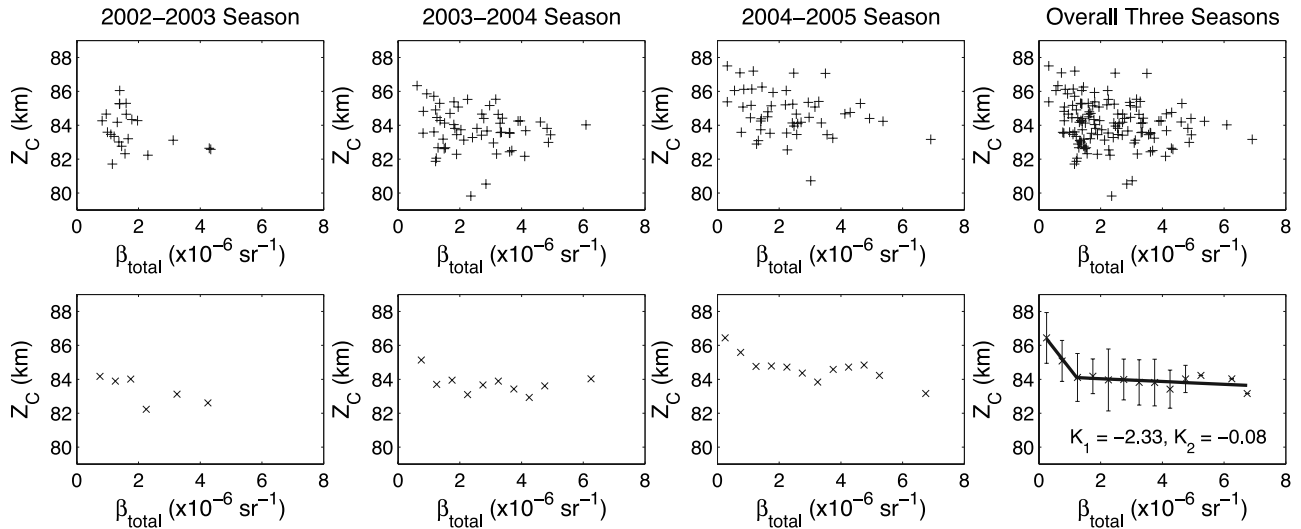


Figure 9. PMC centroid altitude versus total backscatter coefficient (brightness). (All PMC data points in each season and overall three seasons are used in the plots.) (top) Individual data points for each season and overall three seasons together and (bottom) mean altitude averaged in each brightness bin ($0.5 \times 10^{-6} \text{ sr}^{-1}$ per bin). The thin vertical lines in the bottom right plot represent the standard deviations of the PMC altitude in each brightness bins, and the thick solid lines are linear fits to two separate sections of the data (see the text for details).

PMC parameters in Figure 8 are not caused by the solar background variations, but rather true variations in geophysical conditions for PMC formation and development.

3.4. Relationship of PMC Altitude to Brightness

[26] An interesting topic emerging from the above PMC results is the relationship between the PMC altitude and brightness. In Table 2 and Figure 8, it is clearly shown that the phases between altitude and brightness are opposite to each other in the 24-hour, 12-hour, and 8-hour oscillations for most of the cases, except the 8-hour oscillations in the stronger PMC and the 12-hour oscillations in the weaker PMC. In other words, there seems to be an anticorrelation between the PMC altitude and brightness; that is, PMC occurring at higher altitude tend to have lower brightness, just as predicted by the growth-sedimentation-sublimation model [Jensen and Thomas, 1988; Rapp and Thomas, 2006].

[27] To investigate this relationship, PMC brightness (expressed in total backscatter coefficient) is plotted against altitude in Figure 9. The scatterplots of the individual data points are shown in the top row for each season and overall three seasons together. It is striking that the strongest PMC occur at a nearly constant altitude (~ 84 km) in the middle of PMC altitude distribution, rather than at the lowest altitude. For example, in the seasons of 2003–2004 and 2004–2005, although the mean altitudes in these two seasons are quite different from each other, strong PMC occur around 84 km in both seasons. Below and above this altitude, PMC tend to be weaker. This behavior is similar to the results observed at the South Pole where the strongest PMC occur around 85 km (~ 1 km higher than the Rothera constant altitude) and PMC below and above this altitude are weaker [Chu *et al.*, 2003].

[28] To further illustrate the relationship, the individual PMC altitudes are averaged in the brightness bin ($0.5 \times 10^{-6} \text{ sr}^{-1}$), and the results are plotted in the bottom row of

Figure 9. For the overall average illustrated in the bottom and rightmost plot of Figure 9, the thin vertical line on each data point represents the standard deviation of the altitude distribution in each brightness bin, i.e., the geophysical variability of altitude distribution. The relationship of the PMC altitude to brightness exhibits various slopes changing from large negative slopes for weaker PMC to nearly zero slopes for stronger PMC. Similar behavior has been reported by Höffner *et al.* [2003] at Svalbard (78°N) and by Fiedler *et al.* [2003] at Andoya (69°N), where two linear fits were applied to the weaker and stronger PMC separately. In comparison with the Arctic results, two linear fits similar to the ones used by Höffner *et al.* [2003] and by Fiedler *et al.* [2003] are applied to the Rothera overall average data and the results are shown as two thick solid lines in the plot. The limit to divide the weaker and stronger PMC is the total backscatter coefficient of $1.6 \times 10^{-6} \text{ sr}^{-1}$. The slopes are $-2.3 \pm 0.2 \times 10^6 \text{ km}\cdot\text{sr}$ for the weaker PMC and $-0.08 \pm 0.06 \times 10^6 \text{ km}\cdot\text{sr}$ for the stronger PMC. The correlation coefficients for these two fits are 99.5% and 41.5%, respectively.

[29] The slopes given in Fiedler *et al.* [2003] and Höffner *et al.* [2003] are in the dimension of $dz/d\beta_{\text{max}}$ ($\text{km}\cdot\text{m}\cdot\text{sr}$) for 532 and 770 nm, respectively. They must be converted to the dimension of $dz/d\beta_{\text{total}}$ ($\text{km}\cdot\text{sr}$) at 374 nm in order to compare with the Rothera results. Similar to the Gaussian peak assumption made for equation (1), the following equation is used for this conversion:

$$\frac{dz}{d\beta_{\text{total}}(\lambda_{374})} = \frac{1}{R_\lambda} \cdot \frac{\sqrt{8 \ln 2}}{\sqrt{2\pi}FWHM} \cdot \frac{dz}{d\beta_{\text{max}}(\lambda_i)}, \quad (3)$$

where λ_i is the original wavelength 532 or 770 nm for Andoya and Svalbard lidars, and R_λ is the color ratio of 2.28 for 374 nm/532 nm and 7.3 for 374 nm/770 nm in the

Table 3. Fitted Slopes for the Averaged PMC Altitude Versus Brightness^a

	Rothera	Andoya	Svalbard
$K_1, \times 10^6 \text{ km}\cdot\text{sr}$	-2.3 ± 0.2	-0.46	-0.44 ± 0.06
$K_2, \times 10^6 \text{ km}\cdot\text{sr}$	-0.08 ± 0.06	-0.10	-0.017 ± 0.006
Divider, $\times 10^{-6} \text{ sr}^{-1}$	1.6	3.8	4.0

^aFitted slopes are converted to 374 nm. K_1 is the slope for weaker PMC, and K_2 is for stronger PMC. The divider is the total backscatter coefficient limit to divide the data into the weaker and stronger PMC subsets.

assumption of lognormal distribution of spherical PMC particles with a median radius of 40 nm and a width of 1.4 [Höffner *et al.*, 2003]. The converted slopes at 374 nm are $-0.46 \times 10^6 \text{ km}\cdot\text{sr}$ for weak PMC and $-0.10 \times 10^6 \text{ km}\cdot\text{sr}$ for strong PMC at Andoya, while $-0.44 \pm 0.06 \times 10^6 \text{ km}\cdot\text{sr}$ for weak PMC and $-0.017 \pm 0.006 \times 10^6 \text{ km}\cdot\text{sr}$ for strong PMC at Svalbard. Table 3 summarizes the comparison of the two-slope behaviors among Rothera, Andoya, and Svalbard. For the strong PMC, the slopes at Rothera and Andoya are similar but both are much larger than at Svalbard. For the weak PMC, the Rothera slope is much larger than at both northern sites. As discussed below, this two-slope behavior is actually a reflection of the logarithmic relationship between the PMC altitude and brightness, and the differences in slopes are caused by the different PMC brightness.

4. Discussion

[30] The following themes will be discussed regarding the results obtained above: the relationship between the brightness and altitude, the distribution of centroid altitude, the interannual variations and the 8-hour terdiurnal oscillations in PMC parameters.

4.1. Logarithmic Relationship Between PMC Altitude and Brightness

[31] Although Fiedler *et al.* [2003] and Höffner *et al.* [2003] describe a two-slope, linear relationship of the PMC altitude to brightness, the individual data points of Höffner *et al.* [2003] and those presented here in Figure 9 suggest that a continuous logarithmic relationship describing the entire PMC distribution may be more appropriate. Such a relationship could arise from the vertical shifting of PMC particles by the average updraft present during the polar summer. The terminal fall velocity of a particle of a given size, and hence brightness, as a function of atmospheric pressure has been derived by Reid [1975] for particle collisions with the ambient atmosphere that are purely specular, and by Turco *et al.* [1982] for the more general case of a mixture of specular and diffuse reflections. Vertical velocities associated with the cold polar summer mesopause or the action of tides and gravity waves can exceed the fall speed for smaller particles, leading to their upward motion while larger particles continue to fall. This will then concentrate particles of a particular size at the altitude at which the particle fall speed is equal to the average atmospheric ascent rate [Rozenfeld, 1986]. The relationship between atmospheric ascent rate, w , and particle size, r , for these concentrated particles may be expressed as [Turco *et al.*, 1982; Rozenfeld, 1986]:

$$w = \frac{g \cdot \rho_{ice} \cdot r}{V_{th} \cdot \rho_{air} \cdot [1 - \alpha(1 - \pi/8)]}. \quad (4)$$

In the above expression, ρ_{ice} is the mass density of ice, ρ_{air} is the atmospheric mass density at the altitude at which the particles of radius, r , are concentrated, V_{th} is the thermal velocity of the atmosphere at this altitude, g is the gravitational acceleration, and α is the accommodation coefficient that represents the fraction of diffuse collisions [Espy and Jutt, 2002]. The above expression reduces to that of given by Reid [1975] and Chu *et al.* [2003] in the special case of purely specular gas-particle collisions for which $\alpha = 0$.

[32] The atmospheric mass density can be expressed as an exponential function of the altitude as

$$\rho_{air} = \rho_0 \exp[-(z - z_0)/H], \quad (5)$$

where ρ_0 is the mass density at a reference altitude of z_0 , H is the scale height in the mesopause region, and z is the altitude at which the PMC particles of radius, r , are concentrated. Substituting equation (5) into equation (4) and taking the logarithm, we obtain the following relationship between the PMC altitude and its particle radius

$$z = z_0 - H \cdot \ln\left(\frac{g \cdot \rho_{ice} \cdot r}{\rho_0 \cdot w \cdot V_{th} \cdot [1 - \alpha(1 - \pi/8)]}\right). \quad (6)$$

The PMC brightness is generally proportional to the fifth to sixth order of the particle radius, so that the total backscatter coefficient, β_{total} , may be written as

$$\beta_{total} \propto \sum_i r_i^\delta n_{ice}(r_i) \approx A(r_{eq})^d, \quad (7)$$

where r_i is the radius of each individual ice particle, $n_{ice}(r_i)$ is the number density for particles with the radius of r_i , and δ is the power of brightness dependence on the radius. The sum is taken over all available ice particle radii, and an equivalent radius r_{eq} may be used to characterize the total brightness in equation (7), where d is the power and A is an amplitude coefficient. The r_{eq} can be regarded as the mean radius of the PMC particle, r . Substituting equation (7) into equation (6), we obtain the following relationship between the PMC altitude and brightness:

$$z = z_0 - H \cdot \ln\left(\frac{\rho_{ice} \cdot g \cdot (\beta_{total}/A)^{1/d}}{\rho_0 \cdot w \cdot V_{th} \cdot [1 - \alpha(1 - \pi/8)]}\right). \quad (8)$$

[33] Equation (8) is of the form

$$z = c_0 - \frac{H}{d} \cdot \ln(\beta_{total}), \quad (9)$$

where

$$c_0 = z_0 - H \cdot \ln\left(\frac{\rho_{ice} \cdot g}{\rho_0 \cdot w \cdot V_{th} \cdot [1 - \alpha(1 - \pi/8)]}\right) + \frac{H}{d} \cdot \ln(A). \quad (10)$$

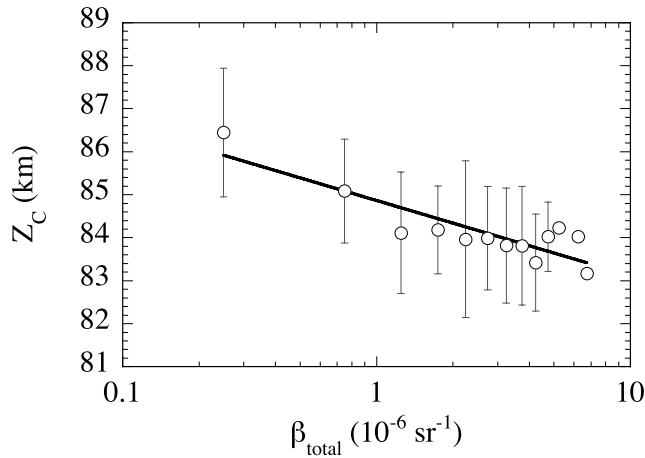


Figure 10. Logarithmic relationship between the averaged PMC altitude and brightness. These data are the same as shown in the bottom right plot of Figure 9. A logarithmic relationship given by equation (9) was applied to the data, and the fitted equation is $z = 74.4 - 0.76 \cdot \ln(\beta_{total})$ with a correlation coefficient of 87.9%. The thin vertical lines represent the standard deviations of the PMC altitude in each brightness bins, and the thick lines are the fitted results in a semilogarithmic scale.

Here, z_0 , ρ_0 , A , and d are constants, while ρ_{ice} , H , g , and V_{th} are weakly dependent on the altitude, z . To the first-order approximation, the averaging done in the second row of Figure 9 reduces these quantities to their average values in the PMC region during summer. Similarly, the vertical velocity, w , is not only weakly dependant on altitude, but also varies about its mean value according to the wave motion present. The vertical wind associated with tides or waves can be on the order of 10 cm/s, compared to the typical mean vertical wind of 3–5 cm/s in summer. This perhaps accounts for the large amount of scatter points seen in the first row of Figure 9. However, the temporally incoherent averaging done in the second row of Figure 9 reduces w to its summertime mean, yielding a c_0 that is approximately constant and a logarithmic relationship between the PMC altitude and total brightness given by equation (9).

[34] *Espy and Jutt* [2002] have modeled the altitude at which particles of a specific radius will be concentrated by a vertical updraft and shown it to bear a logarithmic relationship to the particle radius. To verify this relationship for the present data, we fit a function of the form of equation (9) to the averaged altitude vs. brightness curve given in Figure 9. The resulting fit, $z = 74.4 - 0.76 \cdot \ln(\beta_{total})$, is shown by the solid lines in Figure 10. The quality of the fit is reflected in the correlation coefficient, 88%, and indicates that this single functional form is capable of describing the entire brightness distribution with altitude. The fitted parameters in equation (9) are $c_0 = 74.4 \pm 1.6$ and $H/d = 0.76 \pm 0.12$. The average scale height given by the MSISE00 atmosphere number density data at Rothera in the austral summer (December to January) is about 5 km in the range of 80–90 km. Using this number and the fitted number of H/d , we estimate that $d = 6.6 \pm 1.0$. This is close to theoretically derived power (5–6) for brightness dependence on the

mean particle radius for backscattering observations. However, initial tests on the South Pole data have shown the slope (H/d) to be considerably smaller than that found at Rothera and the derived power d to be very large for the South Pole compared to theoretical values. Thus cautions must be taken when applying the above logarithmic relationship to PMC data obtained at sites other than Rothera, as equation (7) may have oversimplified the problem.

[35] This anticorrelation between the PMC altitude and brightness is consistent with the CARMA model prediction [*Rapp and Thomas*, 2006] when considering the PMC particles in the steady state atmosphere using an updated growth-sedimentation-sublimation model. The averaged altitudes in the brightness bins reflect the PMC properties in the steady state atmosphere as the tides and waves are largely averaged out. Thus, in the steady state, for given size of particles, the PMC altitude is mainly determined by the mean upward vertical wind, w , as given by equation (6). The averaged PMC altitude has a logarithmic relationship to the brightness bins as given by equation (9), and this indicates the anticorrelation between the PMC altitude and brightness in the steady state atmosphere.

[36] With the relationship given by equation (9), the slope of the altitude versus brightness is given by

$$k = \frac{\partial z}{\partial \beta_{total}} = -\frac{H}{d} \cdot \frac{1}{\beta_{total}}. \quad (11)$$

Thus, for weak PMC with low brightness, the slope is a large negative number, while for strong PMC with high brightness, the slope is nearly zero but still slightly negative, just as observed at all three sites mentioned above. Regarding the slope differences among these three sites, they are caused by the different PMC brightness at these sites. The brightness divider used at Rothera is much smaller than the ones used at Andoya and Svalbard; thus the PMC brightness in the weak PMC case is much smaller at Rothera. This results in the slope for weak PMC at Rothera being much larger than the ones observed at these two northern sites. On the other hand, the brightness for strong PMC at Svalbard (78°N) is much larger than those for strong PMC at Rothera (67.5°S) and Andoya (69°N), resulting in the much smaller slope (nearly zero) at Svalbard, as noted above.

4.2. Symmetric Distribution of PMC Centroid Altitude

[37] Regardless of the brightness of the observed PMC, the histogram distribution of PMC altitude is a symmetric Gaussian, as shown in Figure 1 (the overall three seasons distribution). This can be further proved by the test of skewness and kurtosis of the distribution of individual PMC altitudes (unbinned). Skewness is the third moment and characterizes the degree of asymmetry of a distribution around its mean. It is usually defined as [*Press et al.*, 1986]

$$Skewness(x_1, \dots, x_N) = \frac{1}{N} \sum_{j=1}^N \left[\frac{x_j - \bar{x}}{\sigma} \right]^3, \quad (12)$$

where \bar{x} is the mean of the values x_1, \dots, x_N , σ is the standard deviation of the distribution, and N is the number of data points. The skewness is zero if the distribution is

perfectly symmetric, e.g., a normal (Gaussian) distribution. The standard error of the skewness for a normal (Gaussian) distribution is approximately $\sqrt{6/N}$ [Press *et al.*, 1986], which is 0.22 for $N = 128$ of Rothera data points. Kurtosis is the fourth moment and measures whether the data are peaked or flat relative to a normal distribution. The conventional definition of the kurtosis is [Press *et al.*, 1986]

$$\text{Kurtosis}(x_1, \dots, x_N) = \left\{ \frac{1}{N} \sum_{j=1}^N \left[\frac{x_j - \bar{x}}{\sigma} \right]^4 \right\} - 3, \quad (13)$$

where the term of -3 makes the value zero for a normal distribution. Data sets with positive kurtosis tend to have a distinct peak near the mean, while data sets with negative kurtosis tend to have a flat top near the mean. The standard error of the kurtosis for a Gaussian distribution is $\sqrt{24/N}$ [Press *et al.*, 1986], which is 0.43 for $N = 128$ of Rothera data. The calculated skewness of Rothera PMC altitude distribution (unbinned) is -0.10 ± 0.22 with 68% confidence interval, and -0.10 ± 0.44 with 95% confidence interval. The calculated kurtosis of Rothera PMC altitude distribution (unbinned) is 0.53 ± 0.43 with 68% confidence interval, and 0.53 ± 0.86 with 95% confidence interval. Because the 95% confidence intervals of skewness and kurtosis include zero, there is no evidence to reject the hypothesis that the PMC altitude distribution is a symmetric Gaussian. With 68% confidence, the kurtosis is slightly positive, which indicates that the altitude distribution is slightly more cusp-shaped than a Gaussian but with a similar width. This is consistent with the Rothera observations that the most probable altitude is at the mean near the center of the distribution. Lidar observations at an Arctic site, Andoya, exhibit similar symmetric distribution of the PMC altitude [Baumgarten *et al.*, 2005], where the most probable altitude is also at the mean (~ 83 km) in the middle of the distribution. SNOE satellite observations show symmetric distributions of the PMC altitudes in both hemispheres with a nearly perfect Gaussian distribution [Chu *et al.*, 2005; S. M. Bailey *et al.*, Interhemispheric differences in polar mesospheric cloud morphology observed by the Student Nitric Oxide Explorer, submitted to *Journal of Atmospheric and Solar-Terrestrial Physics*, 2006]. These results support the observed symmetric distribution of the PMC altitude at Rothera, and indicate that differences in the mean altitudes between different sites may be tested using statistics appropriate for Gaussian distributions.

[38] How to understand this symmetric distribution shown in Figure 1? One way is to regard the PMC occurring at high altitude as the “young” PMC that just form in the coldest region around the mesopause, regard the PMC occurring around the constant altitude of 84 km as the “golden” PMC that have grown to large sizes and sediment from origin locations to the bottom of the supersaturation region, and regard the PMC occurring at low altitude as the “dying” PMC quickly sublimating when dropping below the supersaturation region. In this sense, because of the much shorter sublimation time compared to PMC sedimentation time, the number of “young” PMC observations should be much more than the “dying” PMC. Thus the histogram of PMC centroid altitude plotted in Figure 1

should show more PMC at high altitudes than at low altitudes. Unfortunately, this is not the case in Rothera observations, and the symmetric distribution is unlikely to be explained by the “young-golden-dying” understanding.

[39] Recall that lidars usually detect larger size of PMC particles >30 nm [Rapp and Thomas, 2006], as the backscatter coefficient is proportional to the fifth to sixth power of particle size. Lidars are not sensitive enough to observe the “young” PMC as they just form in the supersaturation region and are not large enough for lidar detection. When PMC are detected by lidar, these ice particles may have existed in the atmosphere for many hours and grown to appreciable sizes. They are most likely be detected at the altitudes where the net upward force compensates the downward gravitational force as given by equations (4) and (8). If the upward vertical wind is not large enough to uphold the large PMC particles, these particles will descend to the bottom of the saturation region through sedimentation. The symmetric distribution of the PMC altitude may reflect the variations of the saturation region around a mean altitude through the season. The altitude of the saturation region (e.g., the isotherm with saturation factor $S = 1$) moves up and down through the season, but has a mean (i.e., the most probable altitude) around 84 km at Rothera and 83 km at Andoya. The variation of the saturation region around the mean altitude is likely to be symmetric, resulting in the symmetric distribution of the observed PMC altitude.

4.3. Causes for Interannual Variations and Terdiurnal Oscillations

[40] The large interannual variations in the PMC altitude and brightness are another interesting topic for discussion. Over the observational periods at the South Pole (1999–2001 summers) and at Rothera (2002–2005 summers), both locations exhibit more than 1 km interannual changes in PMC altitude. The lidar observed PMC heights at South Pole decrease from 1999–2000 to 2000–2001. These results have been confirmed by SNOE satellite observations that show a similar decrease in PMC height during those years at latitudes of 80° [see Bailey *et al.*, 2005, Figure 7]. The Rothera PMC heights show a reversal of this trend from 2003–2004 to 2004–2005. However, although Bailey *et al.* [2005] reported the data in 2002–2003, no satellite PMC altitude data have been published for the 2003–2005 summers against which the Rothera data may be compared.

[41] The lidar at the South Pole observed a large increase in PMC brightness from 1999–2000 to 2000–2001, and these results have also been confirmed by SNOE [see Bailey *et al.*, 2005, Figure 7] and SBUV [DeLand *et al.*, 2003, 2006] satellite observations for those years. The lidar observations at Rothera show a large increase of PMC brightness from 2002–2003 to 2003–2004, but then the brightness in 2004–2005 decreases a little compared to the previous season. SBUV shows a nearly linear increase of PMC brightness (expressed in PMC albedo) from summer 2002–2003 through the 2004–2005 summer at latitudes between 64°S to 74°S (M. T. DeLand, Science Systems and Applications Inc., private communication, 2006). The PMC extinction observed by HALOE at 67.5°S also shows a large increase from 2002–2003 to 2003–2004 [Hervig and Siskind, 2006], consistent with lidar observations at Rothera (67.5°S). Unfortunately, it is not possible to compare the

final season of Rothera data with HALOE as the HALOE 2004–2005 data have not yet been published.

[42] What causes the large interannual variations in the PMC altitude and brightness? *Chu et al.* [2003] pointed out that $\sim 6\%$ solar flux difference between the Southern and Northern hemispheres could cause 1 km difference in the altitude of the mesopause and the bottom of the saturation region between the two hemispheres. *Siskind et al.* [2005] studied the change of PMC altitude and brightness from solar flux maximum to solar flux minimum using a 2D global chemical/dynamical model coupled with the CARMA PMC model. Their results indicate that the clouds tend to be at higher altitudes in solar max relative to solar minimum. This is due to two factors: the slightly higher altitude of the 150 K isotherm in the solar max, which drives the sublimation of the PMC, and the smaller PMC particles due to less H_2O in the solar max, which fall more slowly thus are detected at higher altitude (*D. Siskind*, Naval Research Laboratory, private communication, 2005). Therefore the solar flux variations could contribute to the observed interannual variations of PMC altitude and brightness. According to the solar Lyman α data from the SOLAR2000 model given in Figure 3 of *Hervig and Siskind* [2006], the solar flux in the season of 2002–2003 is significantly higher than that in the seasons of 2003–2004 and 2004–2005. This is consistent with the model expectation of *Siskind et al.* [2005] in order for the season of 2002–2003 to have a much higher PMC altitude. However, the solar flux in the season of 2004–2005 is lower than that in 2003–2004, which contradicts the model expectation. In addition, the solar flux in 1999–2000 is lower than that in 2000–2001; thus lower PMC altitude is expected in 1999–2000, which also contradicts the observational results at the South Pole. Studies have shown that the anticorrelation between solar flux and PMC brightness is strong on average, but may not be perfect on a year-to-year basis [*DeLand et al.*, 2003]. There exists an apparent phase lag between solar activity and PMC response [*DeLand et al.*, 2003; *Hervig and Siskind*, 2006]. Therefore the solar flux variation may not be solely responsible for the observed interannual variations. The question whether gravity wave variations [*Siskind et al.*, 2003] or other factors cause such large interannual variations remains open. Further modeling efforts and observational data of the temperature, water vapor, and vertical wind in the polar summer mesosphere are needed.

[43] Our data suggest that the 8-hour terdiurnal oscillation is a strong feature in the PMC altitude and brightness observed at Rothera. Diurnal behaviors of PMC brightness and altitude were also observed by lidars at Andoya [*von Zahn et al.*, 1998; *Fiedler et al.*, 2005], and at the South Pole [*Chu et al.*, 2001b, 2003]. At Andoya (69°N), semidiurnal oscillation dominates both the brightness and altitude in 1997 [*von Zahn et al.*, 1998], but the average over 7 years from 1997 to 2003 shows similar amplitudes of diurnal and semidiurnal oscillations [*Fiedler et al.*, 2005]. At the South Pole, diurnal and semidiurnal oscillations have similar weights [*Chu et al.*, 2003]. In overall seasonal mean data over multiple year average, neither of these two locations shows clear 8-hour oscillations, although the 8-hour oscillation was shown on one day at the South Pole and in some individual years at

Andoya as mentioned earlier [*Chu et al.*, 2003; *Fiedler et al.*, 2005]. Terdiurnal atmospheric tides have been previously reported by *Smith* [2000] in meridional and zonal winds at 95 km using HRDI data on UARS satellite, and by *Forbes et al.* [2006] in mesosphere temperature up to 86 km using MLS data on UARS, both near Rothera latitude. The 8-hour oscillation of PMC observed at Rothera may be attributed to the terdiurnal tides. The 8-hour oscillation at the South Pole could be very different from the 8-hour oscillation at Rothera, as classical tides have zero amplitude at the pole. Detailed analysis of these terdiurnal oscillations and their relations to temperature, wind and water vapor variations are out of the scope of this paper. Furthermore, at Sondrestrom (67°N), a northern location with latitude similar to Rothera, PMC does not show a clear tidal signature [*Thayer et al.*, 2003]. *Thayer et al.* [2003] suggest that Sondrestrom is in a gravity wave dominated region, so the gravity wave effect may overwrite the tidal effect. This seems to be a mystery, as Rothera's location is also near mountains and ocean waves; thus it is expected to also be in gravity wave domain. Does the difference between Rothera and Sondrestrom indicate very different gravity wave activities at these two locations or some hemispheric difference? These issues are under investigations.

5. Conclusions

[44] Polar mesospheric clouds were observed by an iron Boltzmann lidar at Rothera, Antarctica from 2002 to 2005. In these three summer seasons, the earliest PMC was detected on 19 November and the latest one was recorded on 2 February, which defines PMC season as long as 76 days at this 67.5°S southern latitude. Overall 128 hours of PMC were detected among the 459 hours of observations, giving a mean occurrence frequency of 27.9% at Rothera. The mean PMC centroid altitude is 84.12 ± 0.12 km, the mean PMC total backscatter coefficient is $2.34 \pm 0.11 \times 10^{-6} \text{ sr}^{-1}$, and the mean layer RMS width is 0.93 ± 0.03 km. The distribution of PMC centroid altitude over all three seasons is symmetric with a nearly Gaussian distribution. The most probable altitude (~ 84 km) occurs at the mean near the center of the distribution. The mean PMC altitude and the symmetric altitude distribution at Rothera support the earlier lidar findings of the hemispheric difference in PMC altitude and the latitudinal dependence of PMC altitude. PMC in the Southern Hemisphere is about 1 km higher than corresponding northern PMC at the same latitude, while higher PMC occurs at higher latitude in both hemispheres with an ascending rate of 39 ± 8 m/deg.

[45] Interannual, seasonal and diurnal variations were observed in the PMC altitude, brightness, and occurrence frequency at Rothera. Mean PMC altitude varies about 1 km from one year to another. Large interannual variations also occur in the PMC occurrence frequency from 2002–2003 through 2004–2005. There is no clear seasonal trend in the PMC brightness. However, the PMC altitude decreases from its maximum around the summer solstice to a minimum around 20–30 days after the solstice and then increases again. Diurnal (24-hour), semidiurnal (12-hour) and terdiurnal (8-hour) variations occurred in PMC altitude

and brightness at Rothera, with the largest amplitude in diurnal variation and smallest in semidiurnal variations. The 8-hour oscillations are clearly shown in PMC altitude and brightness, indicating a unique feature at this southern location.

[46] The observed relationship between the individual PMC altitude and brightness shows that PMC brightness peaks around a nearly constant altitude around 84 km, and PMC below and above this altitude tend to be weaker. The mean PMC altitudes averaged in brightness bins are anticorrelated with the PMC brightness at Rothera, where weaker PMC occur at higher altitude and stronger PMC occur at lower altitude. This is consistent with the CARMA model predictions when considering the PMC particles in the steady state atmosphere using the updated growth-sedimentation-sublimation model. At Rothera, the averaged PMC altitudes are proportional to the logarithm of the PMC brightness. This logarithmic relationship can be explained by the microdynamics considering the upward force due to the mean upwelling vertical wind, the downward gravitational force, and the PMC particle radius. From the logarithmic relationship and our data, it is possible to infer the power for PMC brightness dependence on the mean particle radius for backscattering observations. Our data show that the PMC brightness is proportional to $(r_{eq})^{6.6 \pm 1.0}$ at Rothera, which is generally consistent with theoretical calculations. However, cautions must be taken when applying this derivation to PMC data obtained at other sites.

[47] Tide- or wave-associated vertical wind could modify the mean vertical wind and offset the PMC altitude, while the PMC brightness could also be affected by tides and gravity waves. Thus individual PMC under the influence of tides and waves could be out of the anti-correlation occurring in the steady state, and exhibit some in-phase relationship as well as the weak brightness at low altitude. The symmetric distribution of PMC altitude is unlikely to be explained by the “young-golden-dying” understanding, but may reflect the variations of the saturation region around a mean altitude through the seasons. The causes of the large interannual variations and terdiurnal variations at Rothera remain unclear. These observational results call for in-depth study of PMC microphysics incorporating more tides and gravity waves as well as more observations of PMC related atmospheric conditions in the polar region.

Appendix A: Procedure to Derive Pure PMC Signals From Two Channels of Fe Boltzmann Lidar

[48] Pure PMC signals were derived from the 374 nm lidar data. The derivation procedure has been described in Appendix A of *Chu et al.* [2003] for the case at the South Pole where there are no considerable atomic iron (Fe) signals in the PMC altitude range in the 374 nm data. However, at Rothera, when the 374 and 372 nm lidar channels are on resonance with atomic Fe transitions, there could be some Fe signals within the PMC altitude range. The Fe signals in the lidar channel at 374 nm must be removed in order to identify the PMC and derive reliable PMC parameters. Below is the procedure used in the Rothera PMC data analysis.

[49] At PMC altitude z , the lidar equation is

$$N_S(z) = \left(\frac{P_L \Delta t}{hc/\lambda} T_a \right) [\beta_R(z) + \beta_{PMC}(z) + \beta_{Fe}(z)] \cdot \Delta z \cdot \left(T_a \cdot \frac{A_R}{z^2} \cdot \eta \right) + N_B. \quad (A1)$$

[50] At Rayleigh normalization altitude z_R (50 km), the lidar equation is

$$N_S(z_R) = \left(\frac{P_L \Delta t}{hc/\lambda} T_a \right) \beta_R(z_R) \cdot \Delta z \cdot \left(T_a \cdot \frac{A_R}{z_R^2} \cdot \eta \right) + N_B, \quad (A2)$$

where $N_S(z)$ and $N_S(z_R)$ are the expected photon counts at PMC altitude z and at Rayleigh normalization altitude z_R , P_L is the laser output power, Δt is the integration time, h is Planck constant, c is the light speed, λ is the laser wavelength, T_a is the one-way transmittance of lower atmosphere at wavelength λ , Δz is the thickness of the range bin, A_R is the receiving telescope aperture area, η is the lidar optical efficiency, β_R , β_{PMC} , β_{Fe} represent the volume backscattering coefficient for Rayleigh (molecule) scattering, PMC (Mie) scattering and iron resonance fluorescence scattering, and N_B is the background photon counts.

[51] From above equations, we have

$$\frac{\beta_R(z) + \beta_{PMC}(z) + \beta_{Fe}(z)}{\beta_R(z_R)} = \frac{[N_S(z) - N_B] \cdot z^2}{[N_S(z_R) - N_B] \cdot z_R^2}. \quad (A3)$$

Since the wavelength difference between 374 and 372 nm channels is so small for Rayleigh and Mie scattering, we assume

$$\beta_{R372}(z) = \beta_{R374}(z), \quad \beta_{PMC372}(z) = \beta_{PMC374}(z), \quad \text{and} \\ \beta_{R372}(z_R) = \beta_{R374}(z_R), \quad (A4)$$

where the subscripts 372 and 374 denote the lidar channels at 372 and 374 nm, respectively.

[52] The relationship of iron signals between the two channels is given by

$$\beta_{Fe372}(z) = K(z) \beta_{Fe374}(z), \quad (A5)$$

where $K(z)$ is determined by the Boltzmann factor and the Fe lidar effective cross sections [*Chu et al.*, 2002]. MSISE00 model temperature was used in computing $K(z)$.

[53] By taking the difference between 372 and 374 nm channels, 374 nm Fe signals can be derived as

$$\beta_{Fe374}(z) = \frac{1}{K(z) - 1} \{ [\beta_{R372}(z) + \beta_{PMC372}(z) + \beta_{Fe372}(z)] - [\beta_{R374}(z) + \beta_{PMC374}(z) + \beta_{Fe374}(z)] \} \\ = \frac{1}{K(z) - 1} \cdot \left\{ \frac{[N_{S372}(z) - N_B] \cdot z^2}{[N_{S372}(z_R) - N_B] \cdot z_R^2} \cdot \frac{[N_{S374}(z) - N_B] \cdot z^2}{[N_{S374}(z_R) - N_B] \cdot z_R^2} \right\} \cdot \beta_{R374}(z_R). \quad (A6)$$

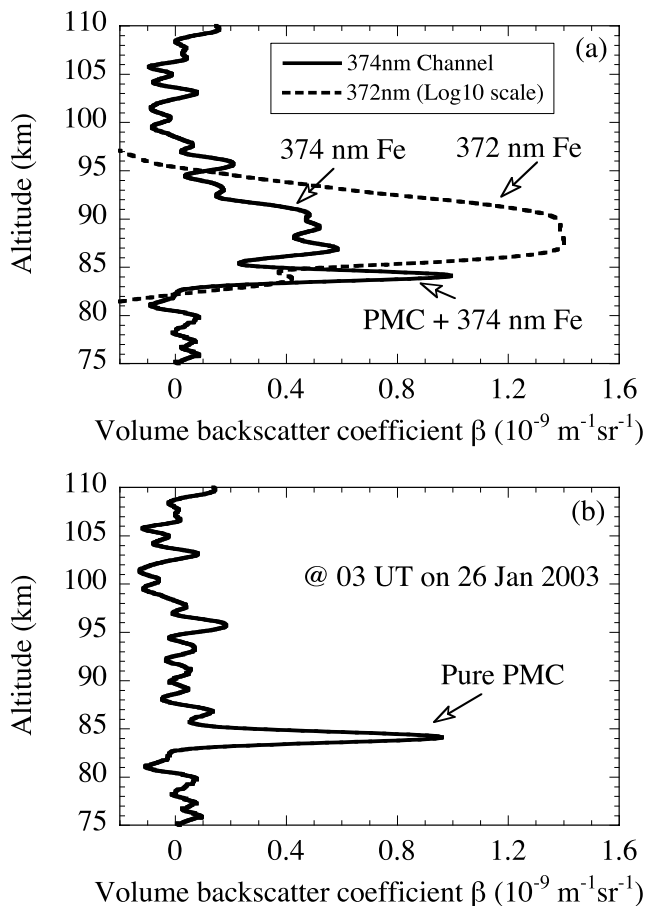


Figure A1. PMC identification from the Fe Boltzmann lidar signals. (a) Total lidar signals consisting of both PMC and Fe when both lidar channels are on resonance. The 372 nm channel (dashed line) is plotted in \log_{10} scale. (b) Pure PMC signal from the 374 nm channel after the Fe signal is removed. This plot demonstrates that subtraction of the 374 nm Fe signal from total lidar signals helps identify PMC and derive precise PMC parameters.

The removal of 374 nm Fe signal was added to the South Pole algorithm described by *Chu et al.* [2003], so the pure PMC volume backscatter coefficient can be obtained from

$$\beta_{PMC}(z) = \left\{ \frac{[N_S(z) - N_B] \cdot z^2}{[N_S(z_R) - N_B] \cdot z_R^2} - \frac{n_R(z)}{n_R(z_R)} - \frac{1}{K(z) - 1} \right\} \cdot \beta_{R374}(z_R). \quad (\text{A7})$$

An example of the iron subtraction is shown in Figure A1. Figure A1a illustrates the PMC and iron signals in the 374 and 372 nm channels. After the subtraction, iron signals are eliminated from the profile and the pure PMC signal was given in Figure A1b.

[54] **Acknowledgments.** The authors gratefully acknowledge the valuable discussions with Gary Thomas and Scott Bailey during the preparation of this manuscript. We thank Andrew Klekociuk of the

Australian Antarctic Division for providing us his lidar observational data on PMC altitude at Davis Station. We thank Gary Thomas for providing the SME climatology data of PMC occurrence frequency. We appreciate David J. Maxfield for his superb engineering work to make the lidar observations possible at Rothera. We sincerely acknowledge the staff of the British Antarctic Survey and the Rothera Research Station for their support through the entire campaign at Rothera. The Rothera lidar project was supported by National Science Foundation grants NSF ATM-03-34357 and ATM-06-02334 and by the U.K. Natural Environmental Research Council.

References

- Bailey, S. M., A. W. Merkel, G. E. Thomas, and J. N. Carstens (2005), Observations of polar mesospheric clouds by the Student Nitric Oxide Explorer, *J. Geophys. Res.*, *110*, D13203, doi:10.1029/2004JD005422.
- Baumgarten, G., G. von Cossart, J. Fiedler, and F.-J. Lübken (2005), Multi-annual observation of noctilucent clouds above ALOMAR, *Eos Trans. AGU*, *86*(52), Fall Meet. Suppl., Abstract SA22A-06.
- Berger, U., and U. von Zahn (2002), Icy particles in the summer mesopause region: Three-dimensional modeling of their environment and two-dimensional modeling of their transport, *J. Geophys. Res.*, *107*(A11), 1366, doi:10.1029/2001JA000316.
- Chu, X., C. S. Gardner, and G. Papen (2001a), Lidar observations of polar mesospheric clouds at South Pole: Seasonal variations, *Geophys. Res. Lett.*, *28*, 1203–1206.
- Chu, X., C. S. Gardner, and G. Papen (2001b), Lidar observations of polar mesospheric clouds at South Pole: Diurnal variations, *Geophys. Res. Lett.*, *28*, 1937–1940.
- Chu, X., W. Pan, G. Papen, C. S. Gardner, and J. Gelbwachs (2002), Fe Boltzmann temperature lidar: Design, error analysis, and initial results at the North and South Poles, *Appl. Opt.*, *41*, 4400–4410.
- Chu, X., C. S. Gardner, and R. G. Roble (2003), Lidar studies of inter-annual, seasonal and diurnal variations of polar mesospheric clouds at the South Pole, *J. Geophys. Res.*, *108*(D8), 8447, doi:10.1029/2002JD002524.
- Chu, X., G. J. Nott, P. J. Espy, C. S. Gardner, J. C. Diettrich, M. A. Clilverd, and M. J. Jarvis (2004a), Lidar observations of polar mesospheric clouds at Rothera, Antarctica (67.5°S, 68.0°W), *Geophys. Res. Lett.*, *31*, L02114, doi:10.1029/2003GL018638.
- Chu, X., et al. (2004b), Lidar observations of mesospheric layers in Antarctica, paper presented at IAGA/IAMAS/ICMA International Workshop on Layered Phenomena in the Mesopause Region (LPMR 2004), Int. Comm. on the Middle Atmos., Cambridge, U. K., 14–17 Sept.
- Chu, X., G. Nott, P. Espy, J. Diettrich, S. Bailey, and C. S. Gardner (2005), Systematic lidar study of polar mesospheric clouds at Rothera, Antarctica, *Eos Trans. AGU*, *86*(52), Fall Meet. Suppl., Abstract SA13A-0233.
- DeLand, M. T., E. P. Shettle, G. E. Thomas, and J. J. Olivero (2003), Solar backscattered ultraviolet (SBUV) observations of polar mesospheric clouds (PMCs) over two solar cycles, *J. Geophys. Res.*, *108*(D8), 8445, doi:10.1029/2002JD002398.
- DeLand, M. T., E. P. Shettle, G. E. Thomas, and J. J. Olivero (2006), A quarter-century of satellite polar mesospheric cloud observations, *J. Atmos. Sol. Terr. Phys.*, *68*, 9–29.
- Espy, P. J., and H. Jutt (2002), Equilibrium temperature of water-ice aerosols in the high-latitude summer mesosphere, *J. Atmos. Sol. Terr. Phys.*, *64*, 1823–1832.
- Fiedler, J., G. Baumgarten, and G. von Cossart (2003), Noctilucent clouds above ALOMAR between 1997 and 2001: Occurrence and properties, *J. Geophys. Res.*, *108*(D8), 8453, doi:10.1029/2002JD002419.
- Fiedler, J., G. Baumgarten, and G. von Cossart (2005), Mean diurnal variations of noctilucent clouds during 7 years of lidar observations at ALOMAR, *Ann. Geophys.*, *23*, 1175–1181.
- Forbes, J. M., D. Wu, and X. Zhang (2006), Solar tides as revealed by measurements of mesosphere temperature by the MLS experiment on UARS, *J. Atmos. Sci.*, *63*(7), 1776–1797.
- Hervig, M., and D. Siskind (2006), Decadal and inter-hemispheric variability in polar mesospheric clouds, water vapor, and temperature, *J. Atmos. Sol. Terr. Phys.*, *68*, 30–41.
- Hervig, M., R. E. Thompson, M. McHugh, L. L. Gordley, J. M. Russell III, and M. E. Summers (2001), First confirmation that water ice is the primary component of polar mesospheric clouds, *Geophys. Res. Lett.*, *28*, 971–974.
- Höfner, J., C. Fricke-Begemann, and F.-J. Lübken (2003), First observations of noctilucent clouds by lidar at Svalbard, 78°N, *Atmos. Chem. Phys.*, *3*, 1101–1111.
- Jensen, E. J., and G. E. Thomas (1988), A growth-sedimentation model of polar mesospheric clouds: Comparisons with SME measurements, *J. Geophys. Res.*, *93*, 2461–2473.

- Klostermeyer, J. (1998), A simple model of the ice particle size distribution in noctilucent clouds, *J. Geophys. Res.*, *103*, 28,743–28,752.
- Klostermeyer, J. (2001), Effect of tidal variability on the mean diurnal variation of noctilucent clouds, *J. Geophys. Res.*, *106*, 9749–9755.
- Lübken, F.-J., and J. Höffner (2004), Experimental evidence for ice particle interaction with metal atoms at the high latitude summer mesopause region, *Geophys. Res. Lett.*, *31*, L08103, doi:10.1029/2004GL019586.
- Picone, J. M., A. E. Hedin, D. P. Drob, and A. C. Aikin (2002), NRLMSISE-00 empirical model of the atmosphere: Statistical comparisons and scientific issues, *J. Geophys. Res.*, *107*(A12), 1468, doi:10.1029/2002JA009430.
- Plane, J. M. C., B. J. Murray, X. Chu, and C. S. Gardner (2004), Removal of meteoric iron on polar mesospheric clouds, *Science*, *304*, 426–428.
- Press, W. H., B. P. Flannery, S. A. Teukolsky, and W. T. Vetterling (1986), *Numerical Recipes: The Art of Scientific Computing*, Cambridge Univ. Press, New York.
- Rapp, M., and G. E. Thomas (2006), Modeling the microphysics of mesospheric ice particles—assessment of current capabilities and basic sensitivities, *J. Atmos. Sol. Terr. Phys.*, *68*, 715–744.
- Rapp, M., F.-J. Lübken, A. Müllemann, G. E. Thomas, and E. J. Jensen (2002), Small-scale temperature variations in the vicinity of NLC: Experimental and model results, *J. Geophys. Res.*, *107*(D19), 4392, doi:10.1029/2001JD001241.
- Reid, G. C. (1975), Ice clouds at the summer polar mesopause, *J. Atmos. Sci.*, *32*, 523–535.
- Rozenfeld, S. H. (1986), Relationship between observations in noctilucent clouds and internal gravity waves, in *Collection of Works of the International Workshop of Noctilucent Clouds*, edited by O. A. Avaste, pp. 173–192, Acad. of Sci. of the Estonian SSR, Tallinn.
- Shettle, E. P., G. E. Thomas, J. J. Olivero, W. F. J. Evans, D. J. Debrestian, and L. Chardon (2002), Three satellite comparison of polar mesospheric clouds: Evidence for long-term change, *J. Geophys. Res.*, *107*(D12), 4134, doi:10.1029/2001JD000668.
- Siskind, D. E., S. D. Eckermann, J. P. McCormack, M. J. Alexander, and J. T. Bacmeister (2003), Hemispheric differences in the temperature of the summertime stratosphere and mesosphere, *J. Geophys. Res.*, *108*(D2), 4051, doi:10.1029/2002JD002095.
- Siskind, D. E., M. H. Stevens, and C. R. Englert (2005), A model study of global variability in mesospheric cloudiness, *J. Atmos. Sol. Terr. Phys.*, *67*, 501–513.
- Smith, A. K. (2000), Structure of the terdiurnal tide at 95 km, *Geophys. Res. Lett.*, *27*, 177–180.
- Stevens, M. H., J. Gumbel, C. R. Englert, K. U. Grossmann, M. Rapp, and P. Hartogh (2003), Polar mesospheric clouds formed from space shuttle exhaust, *Geophys. Res. Lett.*, *30*(10), 1546, doi:10.1029/2003GL017249.
- Stevens, M. H., C. R. Englert, M. T. DeLand, and M. Hervig (2005a), The polar mesospheric cloud mass in the Arctic summer, *J. Geophys. Res.*, *110*, A02306, doi:10.1029/2004JA010566.
- Stevens, M. H., R. R. Meier, X. Chu, M. T. DeLand, and J. M. C. Plane (2005b), Antarctic mesospheric clouds formed from space shuttle exhaust, *Geophys. Res. Lett.*, *32*, L13810, doi:10.1029/2005GL023054.
- Thayer, J. P., and W. Pan (2006), Lidar observations of sodium density depletions in the presence of polar mesospheric clouds, *J. Atmos. Sol. Terr. Phys.*, *68*, 85–92.
- Thayer, J. P., M. Rapp, A. J. Gerrard, E. Gudmundsson, and T. J. Kane (2003), Gravity wave influences on Arctic mesospheric clouds as determined by the Sondrestrom, Greenland, Rayleigh lidar, *J. Geophys. Res.*, *108*(D8), 8449, doi:10.1029/2002JD002363.
- Thomas, G. E. (1991), Mesospheric clouds and the physics of the mesopause region, *Rev. Geophys.*, *29*, 553–575.
- Thomas, G. E. (1996), Is the polar mesosphere the miner’s canary of global change?, *Adv. Space Res.*, *18*(3), 149–158.
- Thomas, G. E., J. J. Olivero, M. DeLand, and E. P. Shettle (2003), A response to the article by U. von Zahn, “Are noctilucent clouds truly a miner’s canary of global change?”, *Eos Trans. AGU*, *84*(36), 352–353.
- Turco, R. P., O. B. Toon, R. C. Whitten, R. G. Keesee, and D. Hollenbach (1982), Noctilucent clouds: Simulation studies of their genesis, properties and global influences, *Planet. Space Sci.*, *30*, 1147–1181.
- von Zahn, U. (2003), Are noctilucent clouds truly a “miner’s canary” of global change?, *Eos Trans. AGU*, *84*(28), 261–268.
- von Zahn, U., and U. Berger (2003), Persistent ice cloud in the midsummer upper mesosphere at high latitudes: Three-dimensional modeling and cloud interactions with ambient water vapor, *J. Geophys. Res.*, *108*(D8), 8451, doi:10.1029/2002JD002409.
- von Zahn, U., G. von Cossart, J. Fiedler, and D. Rees (1998), Tidal variations of noctilucent clouds measured at 69°N latitude by groundbased lidar, *Geophys. Res. Lett.*, *25*, 1289–1292.

X. Chu, Cooperative Institute for Research in Environmental Sciences and Department of Aerospace Engineering Sciences, University of Colorado, 216 UCB, CIRES, Boulder, CO 80309-0216, USA. (xinzha.chu@colorado.edu)

J. C. Diettrich and P. J. Espy, Physical Sciences Division, British Antarctic Survey, High Cross, Madingley Road, Cambridge CB3 0ET, UK.

C. S. Gardner, Department of Electrical and Computer Engineering, University of Illinois at Urbana-Champaign, 377 Henry Administration Building, 506 South Wright Street, Urbana, IL 61801, USA.

G. J. Nott, Department of Physics and Atmospheric Science, Dalhousie University, Halifax, NS, Canada B3H 3J5.